Available online at www.sciencedirect.com
ScienceDirect
Acta Materialia 58 (2010) 3131–3161
Acta MATERIALIA
www.elsevier.com/locate/actamat

Changes in internal stress distributions during yielding of square prismatic gold nano-specimens

R.C. Batra [a,*], A.A. Pacheco [b]

[a] Department of Engineering Science and Mechanics, M/C 0219, Virginia Polytechnic Institute and State University, Blacksburg, VA 24061, USA
[b] Universidad del Norte, Department of Mechanical Engineering, Barranquilla, Colombia

Received 19 October 2009; received in revised form 29 January 2010; accepted 30 January 2010
Available online 2 March 2010

Abstract

We use molecular statics simulations with the tight-binding potential to analyze stress evolution in nanosize square prismatic gold specimens of different aspect ratios (length/width) deformed in either simple tension/compression or tension/compression. In the former case atoms on end faces are displaced axially but are free to move laterally, and in the latter case atoms on end faces are restrained from moving laterally during their axial displacement. It is found that the stress distribution in the unloaded reference configuration is non-uniform, and it satisfies the local and the global equilibrium equations. Large values of the von Mises stress and the maximum shear stress occur on atoms located at the third layer beneath the traction free surfaces forming different patterns for specimens loaded in tension and compression. The specimen is assumed to yield when its total strain energy drops noticeably. Maximum values of the von Mises stress and the maximum shear stress at yielding are essentially independent of specimen's length for specimens deformed in tension. For specimens deformed in compression, wave-like patterns of stresses along the axial centroidal axis are observed when the specimen yields.

Keywords: Molecular statics; Stress distributions; Yielding; Instabilities

1. Introduction

Mechanical properties of a structure with one or more dimensions of the order of nanometers are generally different from those of the corresponding macroscopic body. One reason for these differences is the existence of in-plane stresses induced in traction free bounding surfaces and resulting stresses developed in the interior of the body. Atoms on traction free surfaces and on surfaces beneath them have a different environment as compared to those in the specimen interior (bulk atoms). Since there are atoms only on one side of the traction free surface the inter-atomic spacing between atoms near traction free surfaces is altered, generating in-plane stresses that balance the force exerted on them by interior atoms. This has been studied in molecular statics/molecular dynamics (MS/MD) simulations of tensile deformations of nanowires [1,2]. Diao et al. [1] used the modified embedded atom method (EAM) potential [3] to simulate tensile deformations of gold (Au) specimens of square cross-section oriented in the [1, 0, 0] and [1, 1, 1] crystallographic directions, and found that for nanowires oriented in the [1, 0, 0] direction the effective Young's modulus E varied from 42.3 GPa for 3 nm thick to 127 GPa for 1.83 nm thick wires. For a nanowire the magnitude of the compressive stress at an interior point exceeded 1.6 GPa, which is approximately the yield stress in compression for a bulk material.

Using the EAM potential, Gall et al. [4] simulated tensile deformations of rhombic nanowires with axis along the [1, 1, 0] direction and {1, 1, 1} side surfaces, and of multishell nanowires composed of a single atomic chain surrounded by a helix of six atoms. The yielding of the wire was signified by a sharp discontinuity in the average axial stress–average axial strain curve. For a 0.7 (2.2) nm diameter multishell (rhombic) wire the average axial stress and the average axial strain at yield were 13 (3) GPa and 14% (7%),

* Corresponding author. Tel.: +1 5402316051; fax: +1 5402314574.
E-mail address: rbatra@vt.edu (R.C. Batra).

1359-6454/$36.00 © 2010 Acta Materialia Inc. Published by Elsevier Ltd. All rights reserved.
doi:10.1016/j.actamat.2010.01.054

respectively. They pointed out that the initial compressive stresses in the specimen interior cause the experimentally observed asymmetry in the yield stress for a few nanometer diameter specimen deformed in tension and compression.

Diao et al. [2] have proposed that dislocations nucleate at points where the resolved shear stress reaches a material dependent critical value. Isothermal MD simulations at 2 K of tensile and compressive deformations of Au specimens of square cross-section with [1, 0, 0] and [1, 1, 1] axial orientation were performed using periodic boundary conditions in the length direction. For [1, 0, 0] nanowires less than 2.45 nm in thickness some material points in the reference configuration had yielded. With an increase in the axial strain imposed upon the reference configuration of the 4 nm thick nanowire oriented in the [1, 0, 0] direction, the average axial strain and the average axial stress at yield equaled $\sim -4.8\%$ and ~ -0.7 GPa, respectively, in compression, and $\sim 10\%$ and ~ 4 GPa, respectively, in tension. For the same nanowire oriented in the [1, 1, 1] direction the average axial yield stress in tension and compression was ~ 5 GPa. The Schmidt factor for a bulk material at the onset of yield for the most favorable slip system in the [1, 0, 0] nanowire is larger in compression than that in tension, causing the [1, 0, 0] nanowire to yield at a lower value of the axial stress in compression than that in tension. However, the Schmidt factor for the most favorable slip system in the [1, 1, 1] nanowire is larger in tension than that in compression but the residual compressive stresses counteract this effect producing an equal value of the yield stress in tension and compression. Even though Diao et al. [2] found that the critical resolved shear stress does not change appreciably with the cross-sectional area of the nanowire and that it can be used as a criterion for the nucleation of defects, Liu et al. [5] and Miller and Rodney [6] have stated that the slip system with the highest resolved shear stress is not always activated at the yield point.

Zhang et al. [7] using the linear elasticity theory considered effects of the surface and the initial stresses to find analytical expressions for the effective Young's modulus, strains, stresses, and the yield stress in tension/compression for an isotropic circular nanowire. They found that the effective Young's modulus and, in general, elastic constants of the nanowire do not depend upon the residual stresses. Assuming the von Mises yield criterion, they derived an expression for the yield stress in tension and compression which showed that the initial stress induces the asymmetry observed in the yield stress in tension and compression. It was also found that the influence of elastic properties of the surface and of the initial stresses on the effective elastic properties of a nanowire and its yield stress diminish with an increase in the radius of the nanowire. It seems that the assumption of residual stresses being uniform is not realistic for a nanowire.

Refs. [32,33] used the following criteria to delineate local instabilities in shearing, simple shearing, tension/compression and simple tension/compression deformations of Au specimens: (i) a component of the second-order spatial gradients of the displacement field having large values relative to its average value in the body, (ii) the minimum eigenvalue of the Hessian of the local energy of an atom becoming non-positive, (iii) structural changes represented by a high value of the common neighborhood parameter, and (iv) the local atomic acoustic tensor has at least one non-positive eigenvalue. It was found that for the shear and the simple shear deformations, the initiation of the local instability is not accurately predicted by a vanishing of an eigenvalue of the local atomic acoustic tensor. The occurrence of local instabilities is related to one or more components of the second-order spatial gradients of the displacement becoming very large as compared to their average values in the body. For all types of deformations studied, the criterion (ii) with the local energy computed by considering atoms within the shell of radius one atomic spacing centered at the atom whose stability is being studied gave results that generally agreed with those from criteria (i) to (iii).

Here we use the tight-binding (TB) potential [8] and MS simulations to study the evolution of local and average stresses in a system of Au atoms deformed in either simple tension/compression or in tension/compression. The local Cauchy stress tensor is found with Hardy's method [9]. To verify the accuracy of this measure, the divergence of the Cauchy stress tensor is computed at atomic positions by using the modified smoothed particle hydrodynamics (MSPH) method [10]. For a square sample containing $\sim 60{,}000$ atoms, it was found that components of the divergence of the local Cauchy stress tensor vanish everywhere in the system except at the specimen edges. To verify our simulations we have studied isochoric (volume preserving) triaxial tension/compression deformations of an Au cube and have compared computed average stresses and strain energy densities with those of geometrically identical hyperelastic bodies. The stored energy function for the hyperelastic body is derived from the TB potential using the Cauchy–Born rule [11]. The two sets of curves essentially overlap each other.

The von Mises stress and the maximum shear stress at atomic positions where instabilities occur are found to be much larger than their average values in the specimen. Unstable points are identified by the vanishing of eigenvalues of the Hessian of the local energy computed by considering only the degrees of freedom of atoms located within the first shell around the atom whose cohesive energy is being analyzed. This is similar to the approach of Miller and Rodney [6] except that we consider atoms in a sphere of radius equal to the inter-atomic spacing and they considered rectangular domains. Even though some eigenvalues of the local Hessian where instabilities ensue are negative and indeed give a good representation of the distribution of unstable points (dislocations), our goal here is not to propose a criterion for the nucleation of dislocations; this will be studied in a future work.

It is found that unstable points (atoms) located right beneath the traction free surfaces are in zones of high stress gradients. A specimen is assumed to have yielded when there is a sharp drop in the average axial stress–average axial strain curve. For tensile loading, the average yield

stress equals ~5 GPa for specimens with aspect ratios (length/width) varying from 1 to 20. However, the average yield stress in compression differs by 44% for specimens with $L/H = 1$ and $L/H = 20$.

We also delineate effects of different boundary conditions on the end faces of prismatic specimens, and show the existence of permanent strains after a yielded specimen has been completely unloaded. However, there is no residual permanent strain left in a specimen if it is unloaded from a configuration just before the one in which it yielded.

2. The local stress tensor in atomic simulations

There have been several efforts to identify continuum quantities such as stresses and strains in atomistic simulations [11–21]. Starting from statistical mechanics principles, quantities such as temperature, velocity, displacement, pressure, inter-atomic forces and internal energy have been used to describe a system of particles (atoms). Concepts like temperature, kinetic energy, inter-atomic force, moment of inertia, pressure and linear momentum were studied by Clausius, who also proposed the virial stress tensor that is related to the volume average of the Cauchy stress tensor for a system at 0 K.

For a system comprising N atoms at 0 K, the average values $\bar{\sigma}_{\alpha\beta}$ of components of the Cauchy stress tensor can be computed by using the relation [20]

$$\bar{\sigma}_{\alpha\beta} = -\frac{1}{2\Omega^T}\sum_{i=1}^{N}\sum_{\substack{j=1\\ j\neq i}}^{N} f_\alpha^{(ij)} r_\beta^{(ij)}, \tag{1}$$

where Ω^T equals the volume occupied by the system, $f_\alpha^{(ij)}$ equals the component of the interaction force between atoms i and j along the x_α coordinate and $r_\beta^{(ij)}$ the component of the relative position vector between atoms i and j along the x_β coordinate. This expression is equivalent to the configurational part of the virial stress tensor.

The virial stress tensor extends the concept of pressure introduced in statistical mechanics. The general expression for the absolute pressure p for a group of N particles interacting with each other under a potential V, having average kinetic energy $\langle E_k\rangle_\tau$ and contained in a vessel of volume Ω^T is given by [18]

$$p = -\frac{1}{3\Omega^T}\left\langle \sum_{k=1}^{N}\sum_{\substack{j=1\\ j<k}}^{N} \frac{\partial V}{\partial r^{(kj)}} r^{(kj)} \right\rangle_\tau + \frac{2}{3\Omega^T}\langle E_k\rangle_\tau, \tag{2}$$

where $\langle\rangle_\tau$ indicates the average value of a quantity over a period of time τ and $r^{(kj)}$ the magnitude of the relative position vector between particles k and j. For an ideal gas in which there is no interaction among particles except for perfect elastic collisions, the term corresponding to the internal energy V vanishes and the final result is the relation between the pressure in the system and the average kinetic energy $\langle E_k\rangle_\tau$ over a time period τ. The first term on the right-hand side of Eq. (2), containing the derivative of the internal energy with respect to the relative distance between particles, is called the internal virial. Eq. (2) can be rearranged as the averaged value of the internal virial and twice the kinetic energy:

$$p = \frac{1}{3\Omega^T}\left\langle -\sum_{k=1}^{N}\sum_{\substack{j=1\\ j<k}}^{N} \frac{\partial V}{\partial r^{(kj)}} r^{(kj)} + \sum_{k=1}^{N} m^{(k)}\boldsymbol{v}^{(k)}\cdot\boldsymbol{v}^{(k)} \right\rangle_\tau, \tag{3}$$

where $m^{(k)}$ and $\boldsymbol{v}^{(k)}$ equal, respectively, the mass and the velocity vector of atom k. The negative of this quantity, $-p$, is the pressure that the system exerts on walls of the container. The pressure of the system of particles is also defined as one-third of the trace of the average pressure tensor Π:

$$p = \frac{1}{3}trace(\Pi), \tag{4}$$

where

$$\Pi_{\alpha\beta} = \frac{1}{\Omega^T}\left\langle \sum_{k=1}^{N} f_\alpha^{(k)} r_\beta^{(k)} + \sum_{k=1}^{N} m^{(k)} v_\alpha^{(k)} v_\beta^{(k)} \right\rangle_\tau. \tag{5}$$

In Eq. (5) the internal virial is expressed in terms of internal forces to emphasize the dependence of the pressure tensor on the inter-atomic inter-actions. The virial stress tensor σ^* is defined as the negative of the average pressure tensor, i.e., $\sigma^*_{\alpha\beta} = -\Pi_{\alpha\beta}$ [18,22]. Values of components $\sigma^*_{\alpha\beta}$ of the average virial stress tensor are given by

$$\begin{aligned}\sigma^*_{\alpha\beta} &= \frac{1}{\Omega^T}\left\langle -\sum_{k=1}^{N} f_\alpha^{(k)} r_\beta^{(k)} - \sum_{k=1}^{N} m^{(k)} v_\alpha^{(k)} v_\beta^{(k)} \right\rangle_\tau \\ &= \frac{1}{\Omega^T}\left\langle \frac{1}{2}\sum_{k=1}^{N}\sum_{\substack{j=1\\ j\neq k}}^{N} \frac{\partial V}{\partial r^{(kj)}} \frac{r_\alpha^{(kj)} r_\beta^{(kj)}}{r^{(kj)}} - \sum_{k=1}^{N} m^{(k)} v_\alpha^{(k)} v_\beta^{(k)} \right\rangle_\tau.\end{aligned} \tag{6}$$

The local virial stress tensor $\sigma^{*(i)}_{\alpha\beta}$ is given by [23]

$$\sigma^{*(i)}_{\alpha\beta} = \frac{1}{\Omega^{(i)}}\left\langle -m^{(i)} v_\alpha^{(i)} v_\beta^{(i)} + \frac{1}{2}\sum_{\substack{j=1\\ j\neq i}}^{N} \frac{\partial V}{\partial r^{(ij)}} \frac{r_\alpha^{(ij)} r_\beta^{(ij)}}{r^{(ij)}} \right\rangle_\tau, \tag{7}$$

where $\Omega^{(i)}$ equals the volume of the region associated with atom i, i.e., a representative volume containing atom i. The pressure and the stress tensor have two parts, a part which takes into account the internal forces and the other part that contains the linear momentum of the system of particles. The first term on the right-hand side of Eq. (7) involving the tensor product between the linear momentum of a particle and its velocity has been questioned by some authors (e.g., [14,16]). They argue that the linear momentum of particles crossing the surface of a control volume is not related to the Cauchy stress tensor defined in continuum mechanics. Recently, Hoover et al. [22] have performed 2D MD simulations of a group of particles interacting through a harmonic potential subjected to body forces. They show that components of the Cauchy stress

tensor found from analytic solutions in the elasticity theory agree with those computed using the virial stress, the Cauchy stress tensor is indeed the negative of the pressure tensor, and the kinematic part should be included in the computation of the Cauchy stress. This difference of opinions does not affect our results since the systems under study remain at 0 K during the loading process.

Using the local virial stress tensor, and either the hydrodynamic equivalence based on localization functions [9,13,16,24], or the hyperelastic assumption for the material behavior at the atomic scale [17,25], or the direct computation of the traction vector [12,26], or the principle of virtual work [14], one can find an approximation of the local Cauchy stress tensor defined at each atomic position. Here we use the hydrodynamic equivalence between a discrete and a continuous system to find stresses at the atomic level [9,13,24]; see also Ref. [35] for a discussion of Hardy's approach to a system described by a multi-body potential.

In an attempt to describe continuum quantities in terms of properties of a discrete group of particles, Irving and Kirkwood [24] introduced the concept of a point function stress. As for the virial stress, this stress tensor has two contributions: a kinetic contribution that comes from the linear momentum transferred per unit time due to the microscopic (atomic) velocities as viewed from a coordinate system moving with the macroscopic (continuum) velocity at a given point $\boldsymbol{R}$ in space; the other term is the contribution of internal forces to the stress tensor (internal virial). They thus introduced a localization function $\Psi(\boldsymbol{r})$ to compute continuum quantities at a given point $\boldsymbol{R}$ in the domain as the sum of contributions of each particle to that property. The localization function chosen by Irving and Kirkwood is Dirac's delta function $\delta(\boldsymbol{r})$ with $\boldsymbol{r} = \boldsymbol{r}^{(i)} - \boldsymbol{R}$. Hardy [9] has pointed out the following difficulties in implementing the expression for the local stress tensor proposed by Irving and Kirkwood [24]: (i) the validity of the conservation laws for the equivalent continuum appears to depend on a particular ensemble average, (ii) the obtained formula for the configurational part of the stress tensor contains an infinite series that needs to be truncated, and (iii) the difficulty in evaluating an expression that contains Dirac's delta function. Hardy [9] proposed to replace Dirac's delta function by a localization function Ψ (the units of this function are $1/L^3$) that satisfies following conditions [27]:

1. $\Psi(\boldsymbol{r}^{(i)} - \boldsymbol{R})$ has a global maximum at $\boldsymbol{r}^{(i)} = \boldsymbol{R}$.
2. $\Psi(\boldsymbol{r}^{(i)} - \boldsymbol{R}) \to 0$ as $|\boldsymbol{r}^{(i)} - \boldsymbol{R}| \to \infty$.
3. $\Psi(\boldsymbol{r}^{(i)} - \boldsymbol{R})$ is smooth and non-negative.
4. $\int_{\Omega} \Psi(\boldsymbol{r}^{(i)} - \boldsymbol{R}) d\Omega = 1$.

Following Hardy's approach, the linear momentum density $\boldsymbol{p}$ at the position $\boldsymbol{R}$ in a given continuum domain at time t has the form

$$\boldsymbol{p}(\boldsymbol{R}, t) = \sum_{i=1}^{N} m^{(i)} \boldsymbol{v}^{(i)} \Psi(\boldsymbol{r}^{(i)} - \boldsymbol{R}). \tag{8}$$

The partial differentiation of both sides of Eq. (8) with respect to time gives an equation similar to the balance of linear momentum in continuum mechanics. For quasi-static problems the contribution of inertia forces to the linear momentum equation is neglected. Thus, in the absence of body forces, the equilibrium equation at each material point requires the divergence of the Cauchy stress tensor to be zero. The divergence of the Cauchy stress tensor represents the internal force per unit volume (force density) acting at a material point. Taking into account the total force $\boldsymbol{f}^{(i)}$ on each particle (atom), the following equivalence between the force density in the continuum and the atomic system holds:

$$div\boldsymbol{\sigma} = \frac{\partial}{\partial \boldsymbol{R}} \cdot \boldsymbol{\sigma} = \sum_{i=1}^{N} \boldsymbol{f}^{(i)} \Psi(\boldsymbol{r}^{(i)} - \boldsymbol{R}). \tag{9}$$

Since the internal force on a particle comes from its interaction with other particles, i.e., $\boldsymbol{f}^{(i)} = \sum_{\substack{j=1 \\ j \neq i}}^{N} \boldsymbol{f}^{(ij)}$ ($\boldsymbol{f}^{(ij)}$ is the force between particles i and j), and by Newton's third law, $\boldsymbol{f}^{(ij)} = -\boldsymbol{f}^{(ji)}$, Eq. (9) can be written as

$$div\boldsymbol{\sigma} = \frac{1}{2} \sum_{i=1}^{N} \sum_{\substack{j=1 \\ j \neq i}}^{N} \boldsymbol{f}^{(ij)} (\Psi(\boldsymbol{r}^{(i)} - \boldsymbol{R}) - \Psi(\boldsymbol{r}^{(j)} - \boldsymbol{R})). \tag{10}$$

The bond function $B^{(ij)}(\boldsymbol{R})$ between two atoms i and j is defined as [9]

$$B^{(ij)}(\boldsymbol{R}) \equiv \int_0^1 \Psi(\lambda \boldsymbol{r}^{(ij)} + \boldsymbol{r}^{(j)} - \boldsymbol{R}) d\lambda, \tag{11}$$

and represents, for the case of a radial step function, the fraction of the atomic bond between atoms i and j that is contained in a representative volume defined around each material point $\boldsymbol{R}$; only properties of particles (atoms) inside this representative volume are utilized to define continuum quantities at $\boldsymbol{R}$. The extension of this representative volume has to be chosen carefully in order not to smear the local properties or neglect inter-actions with neighboring particles (atoms). Taking the derivative of $\Psi(\lambda \boldsymbol{r}^{(ij)} + \boldsymbol{r}^{(j)} - \boldsymbol{R})$ with respect to λ we get

$$\frac{\partial \Psi(\lambda \boldsymbol{r}^{(ij)} + \boldsymbol{r}^{(j)} - \boldsymbol{R})}{\partial \lambda} = -\boldsymbol{r}^{(ij)} \cdot \frac{\partial \Psi(\lambda \boldsymbol{r}^{(ij)} + \boldsymbol{r}^{(j)} - \boldsymbol{R})}{\partial \boldsymbol{R}}. \tag{12}$$

Integrating both sides of Eq. (12) with respect to λ from $\lambda = 0$ to $\lambda = 1$, we get

$$\Psi(\boldsymbol{r}^{(i)} - \boldsymbol{R}) - \Psi(\boldsymbol{r}^{(j)} - \boldsymbol{R}) = -\boldsymbol{r}^{(ij)} \cdot \frac{\partial B^{(ij)}(\boldsymbol{R})}{\partial \boldsymbol{R}}. \tag{13}$$

Substitution from Eq. (13) into Eq. (10) gives

$$\frac{\partial}{\partial \boldsymbol{R}} \cdot \boldsymbol{\sigma} = -\frac{1}{2} \sum_{i=1}^{N} \sum_{\substack{j=1 \\ j \neq i}}^{N} \boldsymbol{f}^{(ij)} \boldsymbol{r}^{(ij)} \cdot \frac{\partial B^{(ij)}(\boldsymbol{R})}{\partial \boldsymbol{R}}. \tag{14}$$

The solution of Eq. (14) has the general form $\boldsymbol{\sigma} = \boldsymbol{\sigma}^{(p)} + \boldsymbol{\sigma}^{(c)}$, where $\boldsymbol{\sigma}^{(p)}$ is a particular solution and $\boldsymbol{\sigma}^{(c)}$ is a solution of the homogeneous equation $div(\boldsymbol{\sigma}^{(c)}) = \boldsymbol{0}$. A particular solution of Eq. (14) can be derived as follows:

$$\frac{\partial}{\partial \boldsymbol{R}} \cdot \boldsymbol{\sigma}^{(p)} = -\frac{1}{2}\sum_{i=1}^{N}\sum_{\substack{j=1\\ j\neq i}}^{N} \boldsymbol{f}^{(ij)} \boldsymbol{r}^{(ij)} \cdot \frac{\partial B^{(ij)}(\boldsymbol{R})}{\partial \boldsymbol{R}},$$

$$\frac{\partial}{\partial \boldsymbol{R}} \cdot \left(\boldsymbol{\sigma}^{(p)} + \frac{1}{2}\sum_{i=1}^{N}\sum_{\substack{j=1\\ j\neq i}}^{N} \boldsymbol{r}^{(ij)} \otimes \boldsymbol{f}^{(ij)} B^{(ij)}(\boldsymbol{R}) \right) = 0, \tag{15}$$

$$\boldsymbol{\sigma}^{(p)} = -\frac{1}{2}\sum_{i=1}^{N}\sum_{\substack{j=1\\ j\neq i}}^{N} \boldsymbol{r}^{(ij)} \otimes \boldsymbol{f}^{(ij)} B^{(ij)}(\boldsymbol{R}) \tag{16}$$

where $\mathbf{a} \otimes \mathbf{b}$ denotes the tensor product between vectors $\boldsymbol{a}$ and $\boldsymbol{b}$.

Wajnryb et al. [28] have established the uniqueness of the configurational part of the local stress tensor provided that it satisfies the following conditions:

1. The divergence of the stress tensor must be equal to the internal force per unit volume at every point in the domain (in the dynamic case the internal force includes the inertia force).
2. The stress tensor must produce the correct contribution to the equilibrium pressure of the system (see Eq. (3)).
3. The configurational part of the stress tensor must be symmetric.
4. The stress tensor must be a translationally and rotationally invariant function of the position vector $\boldsymbol{R}$ and the atomic position vector $\boldsymbol{r}^{(i)}$.
5. The stress tensor must be invariant under all permutations of particle indices.
6. The stress tensor must be independent of particle interactions such that when particles are linearly arrayed, the direction of the traction vector $\boldsymbol{t}$ shall be parallel to the linear array.

Wajnryb et al. [28] have proved that for $\boldsymbol{\sigma}^{(c)}$ to satisfy these conditions it must be identically zero, and therefore $\boldsymbol{\sigma} = \boldsymbol{\sigma}^{(p)}$. Thus the Cauchy stress tensor for quasi-static problems is given by

$$\boldsymbol{\sigma} = -\frac{1}{2}\sum_{i=1}^{N}\sum_{\substack{j=1\\ j\neq i}}^{N} \boldsymbol{r}^{(ij)} \otimes \boldsymbol{f}^{(ij)} B^{(ij)}(\boldsymbol{R}). \tag{17}$$

Eq. (17) for local stresses can be used in systems with energetics described by multi-body potentials and is not restricted to pairwise potentials [29].

Using Hardy's method Zimmerman et al. [20] compared the local Cauchy stress tensor with the local virial stress tensor and analyzed the influence of two different localization functions. A system of 3072 copper (Cu) atoms with energetics described by the EAM potential was analyzed under simple tensile deformations. Periodic boundary conditions were applied on all bounding surfaces of the specimen with $8 \times 8 \times 12$ unit cells. Two localization functions were used: a radial step function and a cubic function. The averaging volume $\Omega^{(i)}$ in Eq. (17) for each atomic position was taken to be a sphere of radius R_C. It was shown that values of the Cauchy stress computed with the step function decreased to zero as the radius of the averaging volume increased and fluctuations in the normal stress components were significant for R_C equal to the lattice parameter. However, the amplitude of the fluctuations was effectively suppressed to zero by using the cubic spline function as the localization function. They also obtained the oscillatory behavior while computing normal stresses near free surfaces; we note that Hardy's approach reduces the wavelength of these oscillations and keeps the mean value of the normal stress close to zero. There is a lower limit for the spatial resolution when trying to validate the equivalence between a group of atoms and a continuum, and this connection cannot be made for a very small atomic system. When the representative volume increases, i.e., when more particles are used to compute properties at a given material point, components of the Cauchy stress tensor computed by Hardy's method converge to the average values given by Eq. (7) for every choice of the localization function.

Webb et al. [30] have computed the stress field around an edge dislocation embedded in an elastic material using Hardýs method. The EAM potential for aluminum was used in MS simulations of the edge dislocation in a cylindrical disk of radius 40 nm and thickness 4 nm. Displacement boundary conditions consistent with this type of imperfection in an anisotropic crystal were prescribed on the lateral surface of the cylinder while periodic boundary conditions were enforced along the cylinder axis. The specimen was oriented with the {0, 0, 1} family of crystalline planes parallel to the coordinate planes such that the Y-axis was parallel to the cylinder axis and the X-axis parallel to Burgers vector. The stress tensor at each atomic position was computed by defining a representative cylindrical volume. The σ_{xx} distribution was obtained by using Eq. (17) with radial step functions and results compared with analytical solutions from the linear elasticity theory. The two distributions of σ_{xx} agreed well with each other at points far from the core of the imperfection. Close to the core, the solution from the linear elasticity theory diverges while stress components computed from the MS simulation results converged to zero.

We use Eq. (17) and the following cubic spline as the localization function:

$$\boldsymbol{\Psi}(\boldsymbol{R}) = \frac{1}{\pi h^3}\begin{cases} \left(1 - \frac{3}{2}s^2 + \frac{3}{4}s^3\right), & s \leqslant 1, \\ \frac{1}{4}(2-s)^3, & 1 < s \leqslant 2, \\ 0, & \text{otherwise}, \end{cases} \tag{18}$$

$$s = \frac{|\lambda \boldsymbol{r}^{(ij)} + \boldsymbol{r}^{(j)} - \boldsymbol{R}|}{h}, \tag{19}$$

to compute the local Cauchy stress; here h is the smoothing length that determines the size of the compact support of the localization function. A spherical averaging volume of radius $2a$ is defined at each atomic position where a equals the lattice parameter of an Au crystal at 0 K; $2a$ equals the smoothing length of the localization function. The 5-point Gauss quadrature rule was found to be suffi-

cient to evaluate the one-dimensional integral in Eq. (17) since the difference in results computed with five and eight integration points was less than 0.1%. Results computed using an exponential localization function

$$\Psi(\boldsymbol{R}) = \frac{1}{(\sqrt{\pi}h)^3}\exp(-s^2), \tag{20}$$

with $h = a$ were found to be the same as those computed using Eq. (18). It is shown in Ref. [23] that for hydrostatic deformations a smoothing length of $1.02a$ gives good values of the stress tensor at an atomic position.

3. Molecular statics simulations

The MS simulations address homothermal static deformations at 0 K of an atomic system. Here we simulate tensile and compressive deformations of Au square nanospecimens of width $H = \sim 37$ Å and lengths ranging from ~ 37 Å for $L/H = 1$ to ~ 742 Å for $L/H = 20$. The bounding faces of each specimen are aligned with the coordinate planes $\{1, 0, 0\}$, $\{0, 1, 0\}$ and $\{0, 0, 1\}$. For the tension/compression simulations, atoms in the reference configuration located on end faces $Y = Y_{min}$ and $Y = Y_{max}$ are constrained from moving in the X- and the Z-directions, and their Y-displacements are prescribed. For the simple tension/compression simulations, atoms on end faces $Y = Y_{min}$ and $Y = Y_{max}$ and located along the centroidal line parallel to the X-axis are constrained from moving in the Z-direction and atoms on the centroidal line parallel to the Z-axis are constrained from moving in the X-direction, thus allowing all cross-sections of a specimen to expand or contract. In every case, the Y-displacement is prescribed in increments of 0.25 Å, and no external forces in the X- and the Z-directions are applied on atoms at the end faces. Once a discontinuity in the total strain energy vs. the axial strain curve is observed, simulations are restarted from the immediately preceding configuration with the prescribed Y-displacements incremented by 0.1 Å. There are no external forces applied on the four lateral surfaces.

We start numerical simulations by assigning the initial position vector $\boldsymbol{X}_I^{(i)}$ of each atom in the system in a perfect lattice configuration. Without applying any external force, each atom is allowed to move freely till the potential energy of the system has reached a local minimum (within 1×10^{-8} eV Å^{-1}) by using the conjugate gradient (CG) with warranted descent technique of Hager and Zhang [31]. The position vector of an atom in the relaxed configuration is denoted by $\boldsymbol{X}_R^{(i)}$, and this configuration is taken as the reference configuration. After each increment in prescribed displacements of atoms on the end faces of the body, the total potential energy is minimized. The change in the potential energy of the system from that in the reference configuration equals the strain energy of deformation. The process is continued till atoms on the end faces have been displaced by the prescribed amount.

4. Verification of the approach

To verify computations of stresses by Hardy's method we performed MS simulations of the specimens described in Section 3 deformed by prescribing normal displacements on all bounding surfaces, and compared results from MS simulations with those of a hyperelastic body whose strain energy density is derived from the TB potential and the Cauchy–Born rule. Recalling that Poisson's ratio for an Au crystal at 0 K is ~ 0.47, for simplifying the analysis, we consider isochoric deformations of the hyperelastic body. Analytical expressions for components of the average Cauchy stress tensor of the boundary-value problem with the deformation gradient $\boldsymbol{F} = \mathrm{diag}\{\lambda_1, \lambda_2, \lambda_3\}$, where $\lambda_1 = \lambda_3 = 1/\sqrt{\lambda_2}$ can be obtained. Here λ_1, λ_2 and λ_3 are stretches along the x-, the y-, and the z-axes, respectively, in the reference configuration. The first Piola–Kirchhoff stress tensor $\overline{\boldsymbol{P}}$ equals the derivate of the strain energy density with respect to the deformation gradient, i.e.,

$$\overline{\boldsymbol{P}} = \frac{\partial W_0}{\partial \boldsymbol{F}} = \frac{\partial}{\partial \boldsymbol{F}}\left(\sum_{i=1}^{N}\frac{V^{(i)}}{\Omega_R^{(i)}}\right), \tag{21}$$

or equivalently

$$\begin{aligned}\overline{\boldsymbol{P}}_{\alpha\beta} &= \sum_{i=1}^{N}\sum_{\substack{k=1\\k\neq i}}^{N}\frac{1}{\Omega_R^{(i)}}\frac{\partial V^{(i)}}{\partial r^{(ik)}}\frac{\partial r^{(ik)}}{\partial r_\gamma^{(ik)}}\frac{\partial r_\gamma^{(ik)}}{\partial \boldsymbol{F}_{\alpha\beta}}\\ &= \sum_{\substack{i,k=1\\i\neq k}}^{N}\frac{1}{\Omega_R^{(i)}}\frac{1}{r^{(ik)}}\frac{\partial V^{(i)}}{\partial r^{(ik)}}r_\alpha^{(ik)}R_\beta^{(ik)},\end{aligned} \tag{22}$$

where $\Omega_R^{(i)}$ and $R_\beta^{(ik)}$ equal the volume of the region associated with atom i and the component of the relative position vector between atoms i and k along the x_β-coordinate in the reference configuration. From expression (22) and the relation between $\overline{\boldsymbol{p}}$ *and* $\boldsymbol{\sigma}$, we obtain the following for the Cauchy stress tensor:

$$[\bar{\sigma}] = \sum_{\substack{i,k=1\\i\neq k}}^{N}\frac{1}{\Omega^{(i)}}\frac{1}{r^{(ij)}}\frac{\partial V^{(i)}}{\partial r^{(ik)}}[\Theta^{(ik)}(\lambda_1,\lambda_2,\lambda_3)], \tag{23}$$

where

$$[\Theta^{(ik)}(\lambda_1,\lambda_2,\lambda_3)] = \begin{bmatrix}\lambda_1, \lambda_1 R_{xx}^{(ik)} & \lambda_1, \lambda_2 R_{xy}^{(ik)} & \lambda_1, \lambda_3 R_{xz}^{(ik)}\\ \lambda_2, \lambda_1 R_{yx}^{(ik)} & \lambda_2, \lambda_2 R_{yy}^{(ik)} & \lambda_2, \lambda_3 R_{yz}^{(ik)}\\ \lambda_1, \lambda_3 R_{xz}^{(ik)} & \lambda_3, \lambda_2 R_{zy}^{(ik)} & \lambda_3, \lambda_3 R_{zz}^{(ik)}\end{bmatrix},$$

$R_{xy}^{(ik)} = R_x^{(ik)}R_y^{(ik)}, R_{yy}^{(ik)} = R_y^{(ik)}R_y^{(ik)}, \ldots$ Here we have set $\Omega^{(i)} = J\Omega_R^{(i)} = \Omega_R^{(i)}$ since $J = \det[\boldsymbol{F}] = 1$.

For a specimen deformed in tension/compression along the y-axis, Figs. 1a and b and 2 exhibit the evolution with the average axial strain ε of the average axial stress σ_{yy}, the average axial stress σ_{xx} and the strain energy density obtained from MS simulations of deformations. It is clear that prior to the onset of an instability indicated by a sharp drop in σ_{yy}, σ_{xx} and the strain energy density for an infinitesimal increase in ε, results from MS simulations agree

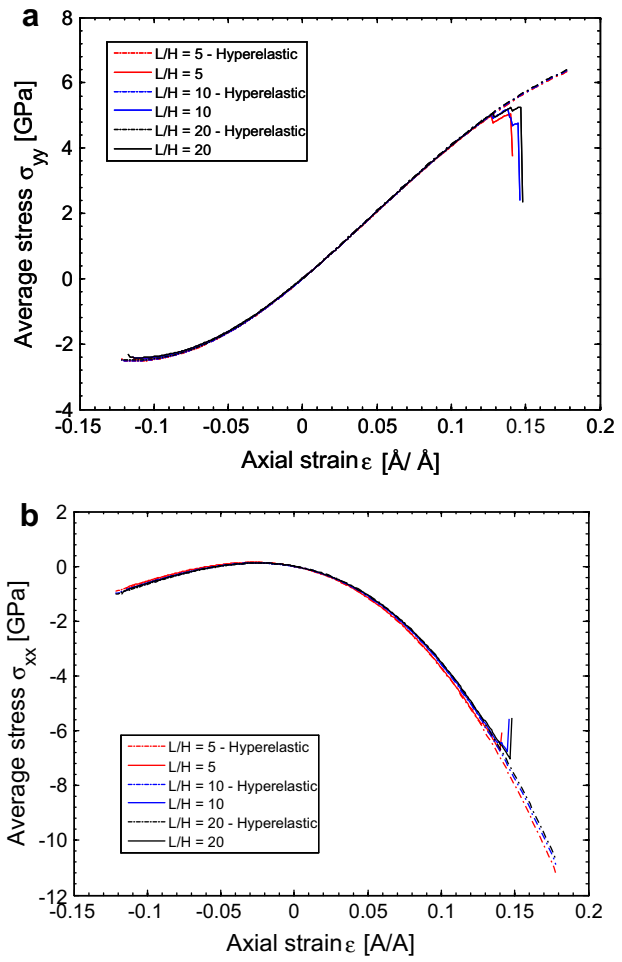

Fig. 1. Variation with the axial strain ε of the average components of the Cauchy stress tensor for tension/compression with essential boundary conditions prescribed on all bounding surfaces ($\boldsymbol{F} = \mathrm{diag}\{\lambda_1, \lambda_2, \lambda_3\}$, where $\lambda_1 = \lambda_3 = 1/\sqrt{\lambda_2}$) for different L/H ratios. (a) σ_{yy}; (b) σ_{xx}.

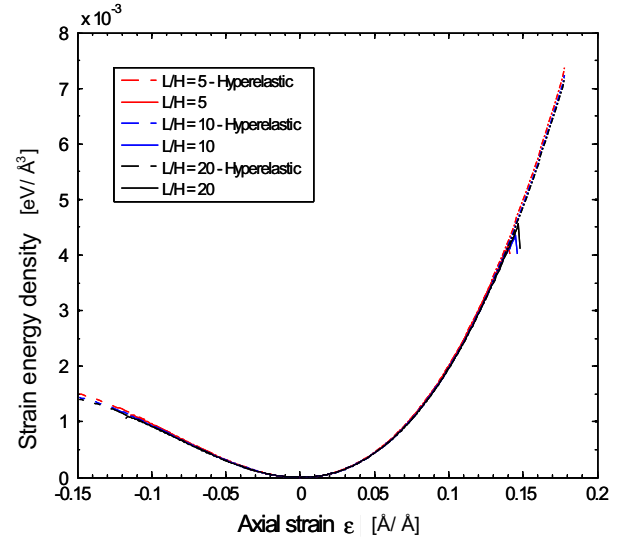

Fig. 2. Variation with the axial strain ε of the strain energy density for tension/compression with essential boundary conditions prescribed on all bounding surfaces ($\boldsymbol{F} = \mathrm{diag}\{\lambda_1, \lambda_2, \lambda_3\}$, where $\lambda_1 = \lambda_3 = 1/\sqrt{\lambda_2}$) for different L/H ratios.

well with those from the analytical solution for specimens with $L/H = 5$, 10 and 20. The close agreement between stresses and the strain energy density computed from results of MS simulations and the analytic expression verifies our use of Hardy's method for computing stresses. A similar close agreement between stresses computed by the two approaches was obtained for simple shearing deformations in Ref. [32].

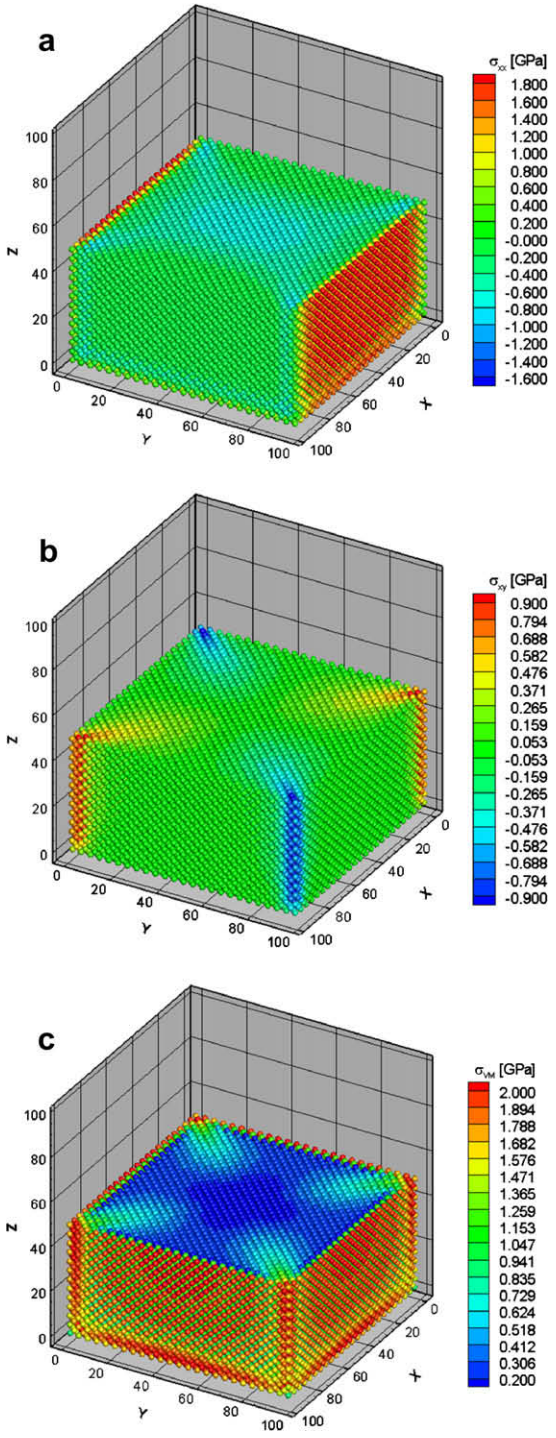

Fig. 3. For a cubic specimen of side 100 Å, distribution in the reference configuration of stresses on the mid-section; (a) σ_{xx}; (b) σ_{xy}; (c) σ_{VM}.

Table 1
For specimens with different L/H ratios, the relative change in the total potential energy (V), the relative change in the total volume (Ω^T), and the axial strain (ε) induced during the minimization of the potential energy of the initial unloaded configuration.

L/H	L (Å)	No. atoms	$\frac{\Delta V}{V_i}$ (eV/eV)	$\frac{\Delta \Omega^T}{\Omega_i^T}$ (Å^3/Å^3)	Axial strain (Å/Å)
1	~32	3480	3.763×10^{-3}	-2.021×10^{-2}	-2.081×10^{-2}
1	~50	7813	2.549×10^{-3}	-1.486×10^{-2}	-1.713×10^{-2}
1	~100	58,825	1.044×10^{-3}	-6.923×10^{-3}	-1.036×10^{-2}
3	~110	9928	2.616×10^{-3}	-1.531×10^{-2}	-1.589×10^{-2}
5	~188	16,787	2.369×10^{-3}	-1.518×10^{-2}	-1.518×10^{-2}
10	~367	32,671	2.197×10^{-3}	-1.361×10^{-2}	-1.469×10^{-2}
20	~742	65,883	2.105×10^{-3}	-1.316×10^{-2}	-1.430×10^{-2}

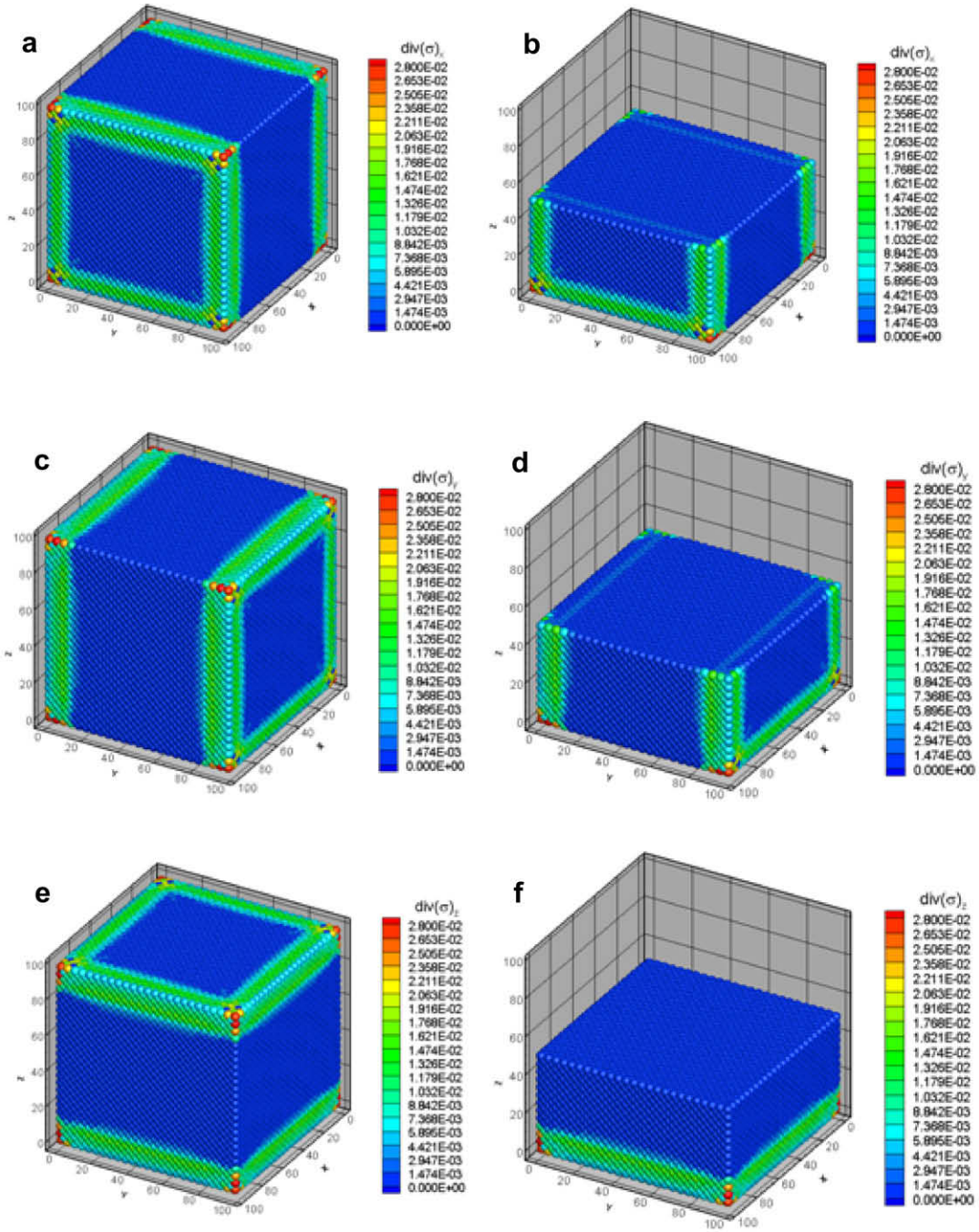

Fig. 4. For a cubic specimen of side 100 Å, distributions of components of $div(\boldsymbol{\sigma})$ on the bounding surfaces and on the mid-section $Z = 50$ Å in the reference configuration; (a) and (b) $(div(\boldsymbol{\sigma}))_x$; (c) and (d) $(div(\boldsymbol{\sigma}))_y$; (e) and (f) $(div(\boldsymbol{\sigma}))_z$.

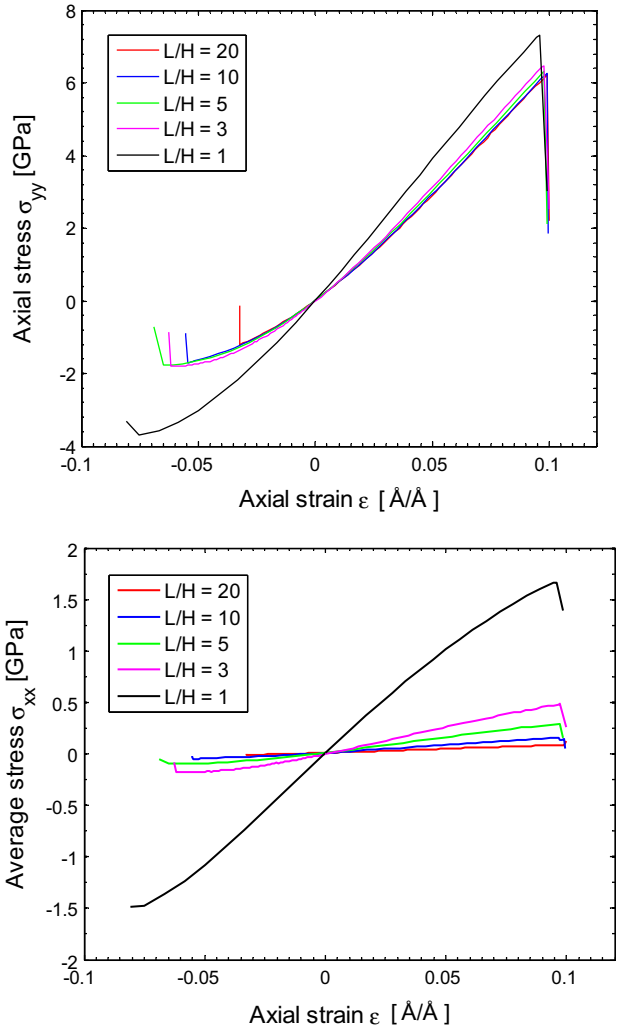

Fig. 5. Evolution with the average axial strain ε of the average values of components of the Cauchy stress tensor for the tension/compression tests for different L/H ratios. (a) σ_{yy}; (b) σ_{xx}.

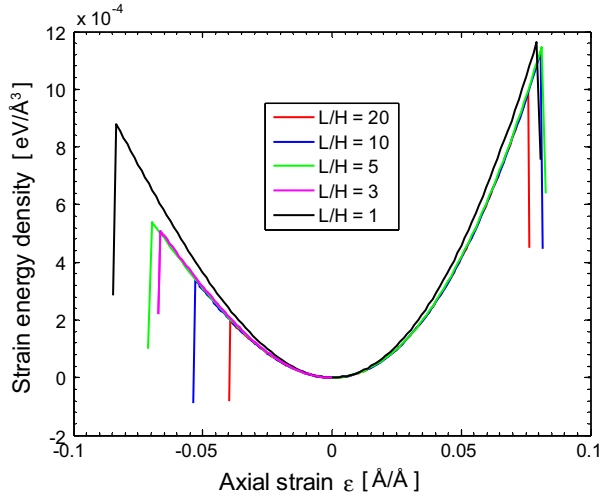

Fig. 6. Variation with the average axial strain ε of the strain energy density in simple tension/compression tests.

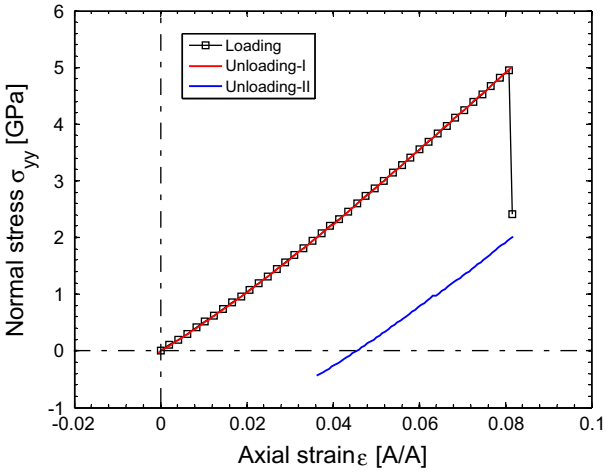

Fig. 7. For $L/H = 10$, variation with the average axial strain ε of the average axial stress for loading and unloading paths in simple tension.

5. Results and discussion

5.1. Stress distribution in the reference configuration

For a cubic specimen of size 100 Å Fig. 3 shows distributions in the reference configuration of components σ_{xx} and σ_{xy} of the Cauchy stress tensor, and the von Mises stress σ_{VM}. The effect of surface tension in bounding surfaces of the specimen is reflected in non-vanishing values of the initial local stresses. The distribution of σ_{xx} in Fig. 3a shows a compressive stress of ~0.5 GPa at the centroid of the specimen; σ_{xx} equals zero on free surfaces perpendicular to the x-axis and has a maximum tensile value

Table 2
Values of the average axial stress and the average axial strain at the yield point for specimens with different L/H ratios deformed in tension and compression.

L/H	Tension		Compression	
	σ_{yy}^{yield} (GPa)	ε_{yy}^{yield} (%)	σ_{yy}^{yield} (GPa)	ε_{yy}^{yield} (%)
1	7.317	9.597	−3.698	−7.789
3	6.481	9.745	−1.783	−6.182
5	6.344	9.809	−1.788	−6.764
10	6.256	9.883	−1.704	−5.460
20	6.242	9.942	−1.209	−3.245

Table 3
Values of the average axial stress and the average axial strain at the yield point for specimens with different L/H ratios deformed in simple tension and compression.

L/H	Simple tension		Simple compression	
	σ_{yy}^{yield} (GPa)	ε_{yy}^{yield} (%)	σ_{yy}^{yield} (GPa)	ε_{yy}^{yield} (%)
1	5.134	7.928	−2.498	−8.345
3	5.050	8.119	−1.784	−6.643
5	4.996	8.117	−1.810	−6.897
10	4.990	8.086	−1.671	−5.157
20	4.618	7.584	−1.387	−3.874

of ~1.8 GPa on the remaining four surfaces. Similar distributions were obtained for σ_{yy} and σ_{zz} components. The shear stress σ_{xy} is zero everywhere in the specimen except at edges parallel to the z-axis where it has a magnitude of ~0.9 GPa. Except for atoms located on the edges, surface tractions at atoms on the bounding surfaces are close to zero and thus satisfy boundary conditions from the continuum mechanics point of view. For atomic level simulations, stresses are defined at atomic locations only, so stresses in the empty space are interpolated values from those at atoms. The distribution of the von Mises stress depicted in Fig. 3c shows that the highest value, ~2 GPa, occurs at points on free surfaces and $\sigma_{VM} = 0.2$ GPa at points on the specimen centroid. Even though the distribution of stresses in the reference configuration is qualitatively the same for the three cubic specimens of sides 32, 50 and 100 Å, their magnitudes differ. For the three cubic and four rectangular specimens, we have listed in Table 1 relative change in the total volume, the relative change in the total potential energy, and the average axial strain (change in length per unit initial length) in the x-direction in going from the initial perfect lattice configuration to the unloaded relaxed (reference) configuration. The total volume of a specimen was computed by adding the Voronoi volume assigned to each atom. Values listed in Table 1 indicate that the average volumetric strain and the average axial strain for the smallest specimen equal ~2%, and are ~1.5% for larger specimens. The change in the total potential energy of a specimen during the minimization of its potential energy is not significant for any one of the seven specimens; it is ~0.37% for the specimen with 3480 atoms and only ~0.1% for the specimen with 58,825 atoms. These geometrical changes are accompanied by the development of residual stresses. For the smallest (largest) cubic sample, $\sigma_{xx} \sim -1.6$ (~−0.5) GPa at the specimen centroid. In order to balance the resultant forces coming from the interior, the space between under-coordinated atoms near bounding surfaces is reduced, causing the outermost layers of the

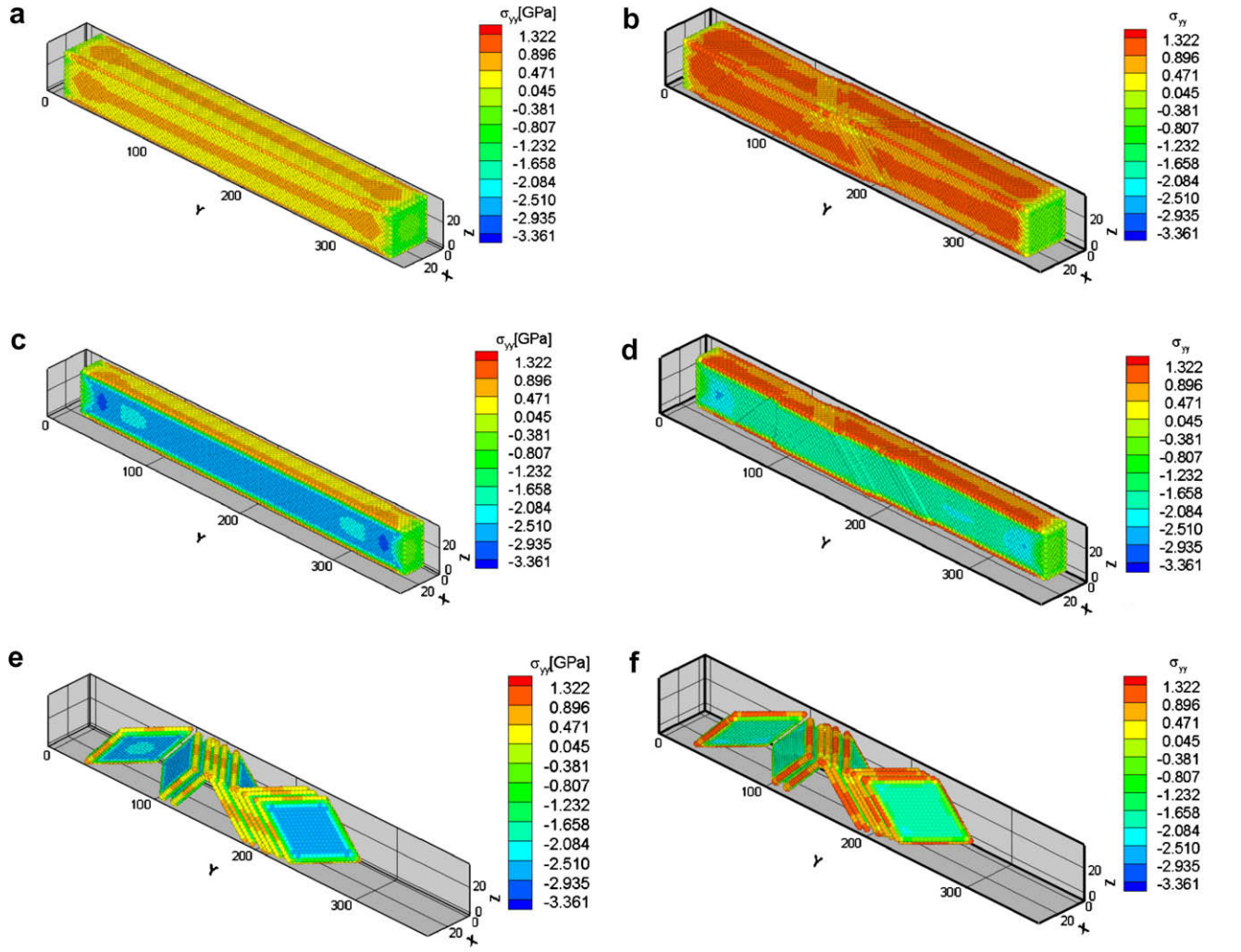

Fig. 8. For simulations of the simple compressive deformations of the specimen with $L/H = 10$, distribution of σ_{yy} component of the local Cauchy stress tensor on (a and b) the bounding surfaces, (c and d) the mid-section, $X = 18$ Å, and (e and f) at points where the minimum eigenvalues of the local Hessian matrix has become negative; for Figs. (a, c and e) $\varepsilon = -5.15\%$; and for (b, d and f) $\varepsilon = -5.16\%$.

specimen to act as membranes that compress the bulk atoms.

We have plotted in Fig. 4a–f the x-, the y- and the z-components of $div(\mathbf{\sigma})$ on the bounding surfaces and on the mid-surface $z = H/2$. It is clear that except for points near the edges, $div(\mathbf{\sigma})$ is nearly zero everywhere, attesting to the satisfaction of the local equilibrium equations in the reference configuration. The gradients of stresses from their values at atomic positions were found by the MSPH method [10] using cubic splines in Eq. (18) as smoothing functions.

5.2. Average stresses and strains from numerical simulations

5.2.1. Tension/compression

For different values of L/H, Fig. 5a, b shows the variation with the average axial strain ε (change in length per unit initial length) of the average values of σ_{xx} and σ_{yy} components of the Cauchy stress tensor. It is observed that the variation with ε of the average σ_{yy} stress is the same for $L/H \geqslant 3$. For $L/H = 1$ all normal stresses are of the same order of magnitude showing a very different behavior as compared to that for samples having $L/H \geqslant 3$. For a square cross-section σ_{zz} equals σ_{xx}. Note that atoms on the end faces are constrained to move axially only; thus these cross-sections do not change. With an increase in L/H, the average values of σ_{xx} and σ_{zz} decrease and are nearly one-tenth of the average value of σ_{yy}. The average values of all shear stresses are negligible till discontinuities in the σ_{yy} vs. ε curve occur. Subsequent to the occurrence of these discontinuities, values of local shear stresses may not be very small and are comparable to the values of the local normal stresses in regions close to edges, vertices of the specimen and places where defects are present. In Table 2 we have listed, for different values of L/H, average values of σ_{yy} and ε at yield identified by a sharp drop in the average axial stress for an infinitesimal increase in the average axial strain. Values of the axial yield stress and the corresponding axial strain for $L/H \geqslant 3$ for tension are $\sim$6.2 GPa and $\sim$9.8%, respectively. However, values of

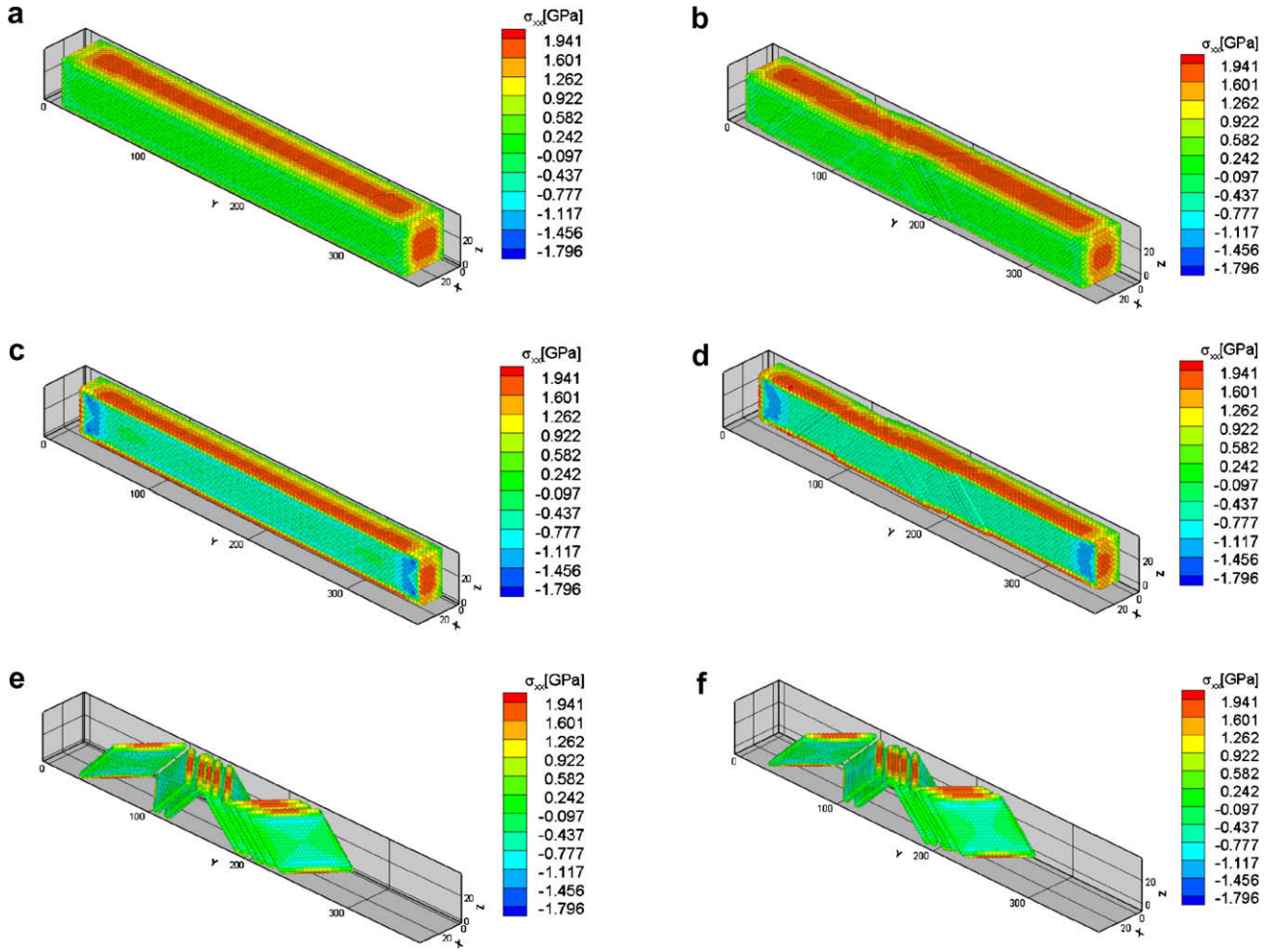

Fig. 9. For simulations of the simple compressive deformations of the specimen with $L/H = 10$, distribution of σ_{xx} component of the local Cauchy stress tensor on (a and b) the bounding surfaces, (c and d) the mid-section, $X = 18$ Å, and (e and f) at points where the minimum eigenvalue of the local Hessian matrix has become negative; for Figs. (a, c and e) $\varepsilon = -5.15\%$; and for (b, d and f) $\varepsilon = -5.16\%$.

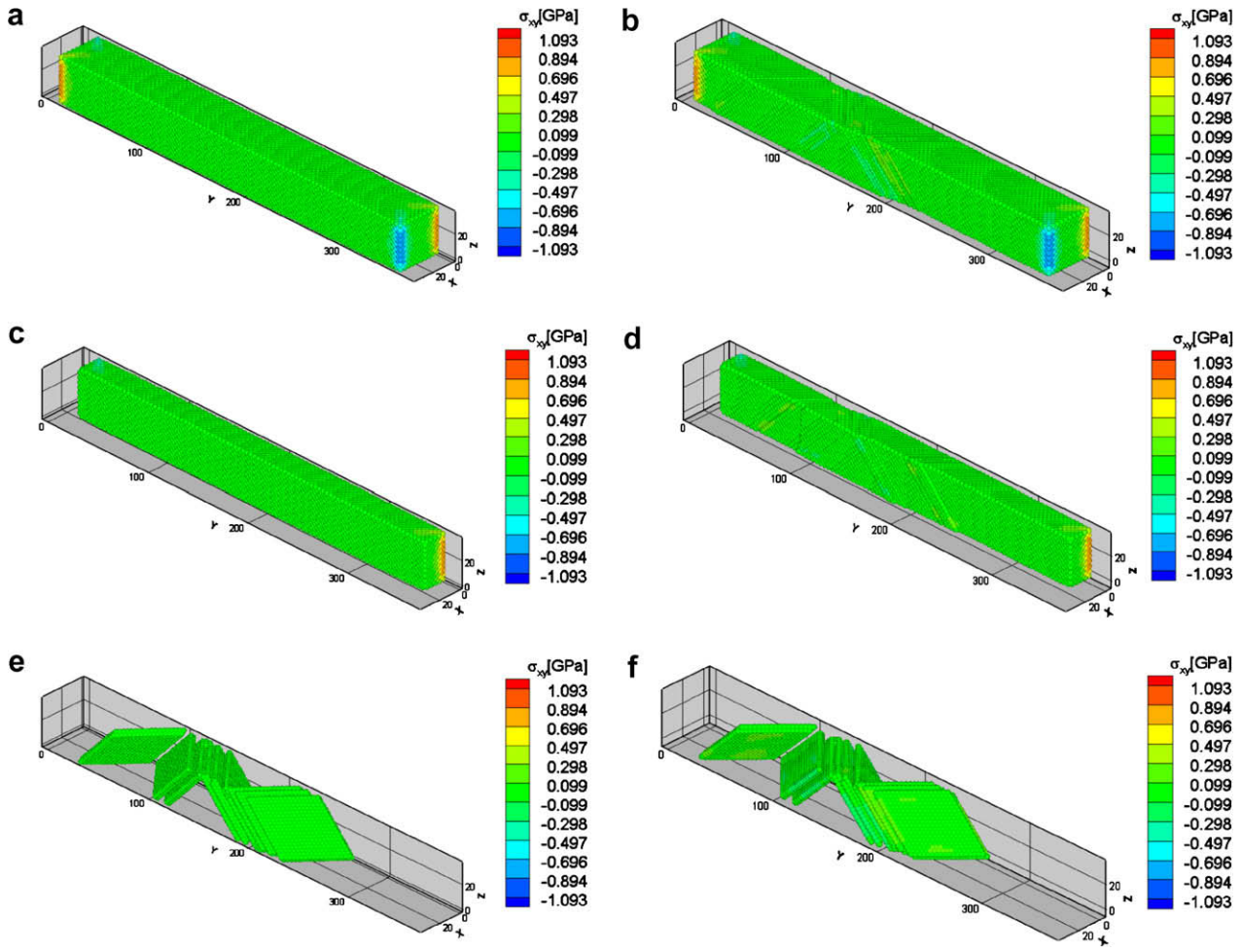

Fig. 10. For simulations of the simple compressive deformations of the specimen with $L/H = 10$, distribution of σ_{xy} component of the local Cauchy stress tensor on (a and b) the bounding surfaces, (c and d) the mid-section, $X = 18$ Å, and (e and f) at points where the minimum eigenvalue of the local Hessian matrix has become negative; for Figs. (a, c and e) $\varepsilon = -5.15\%$; and for (b, d and f) $\varepsilon = -5.16\%$.

the axial stress and the axial strain at the yield point in compression for $L/H = 1$ and 20 differ noticeably from those for $L/H = 3$, 5 and 10.

For the same L/H ratio asymmetry in the yield stress in tension and compression is apparent from values listed in Table 2 as was also found by Diao et al. [1,2], and Zhang et al. [7] This asymmetry is attributed to initial stresses in the reference configurations of specimens. The internal compressive stresses induced by the surface tension cause a local critical stress in compression to be reached at a smaller value of the axial strain than that in an initially stress-free specimen, whereas the average axial stress vs. the average axial strain curve is essentially linear in tension it is nonlinear in compression.

5.2.2. Simple tension/compression

For different values of L/H, as for the simulations of tension/compression deformations, it is observed that the variation with ε of the average value of σ_{yy} is the same for specimens with $L/H \geqslant 3$. However, for the simple tension/compression simulations, the average values of σ_{zz} and σ_{xx} are negligible as compared to the average values of σ_{yy}. The applied boundary conditions allow atoms on the end faces to move freely in the x- and the z-directions; consequently, edge effects are negligible and averaged values of σ_{zz} and σ_{xx} are very small.

Fig. 6 shows the variation with the average axial strain of the strain energy density. The σ_{yy} vs. ε curves (not included here for the sake of brevity) show a discontinuity at the strain level where the strain energy density for the entire system decreases noticeably; it corresponds to the system becoming globally unstable, and we take this as characterizing yielding of the material. The variation of the strain energy density for $L/H = 1$ is different from that for specimens with $L/H \geqslant 3$. For $3 \leqslant L/H \leqslant 20$, the variation with the average axial strain of the strain energy density is essentially independent of the aspect ratio L/H. However, the yield stress in simple compression depends noticeably upon the value of L/H.

In Fig. 7 we have plotted the average axial stress vs. the average axial strain during unloading from two configurations – one just before the drop in the average axial stress

vs. the average axial strain curve and the other just after this drop. When the specimen is unloaded from the configuration just before the average axial stress drops noticeably, the average axial stress vs. the average axial strain curve during unloading overlaps that during loading suggesting that the specimen deformed elastically. However, when the specimen is unloaded by reversing the direction of prescribed axial incremental displacements from the configuration just after the severe drop in the axial stress or the strain energy density, there is a residual average axial strain at zero average axial stress. It confirms that the specimen deformed plastically during the instant the average stress dropped.

As in the tension/compression tests the average values of all shear stresses are negligible up to the discontinuity in the σ_{yy} vs. ε curves. In Table 3 we have listed, for different L/H ratios, values of the average σ_{yy} stress and the average axial strain at the yield point. Values of the average axial stress and the average axial strain at yield for $10 \geqslant L/H \geqslant 3$ for the simple tension case are ~5 GPa and ~8% respectively; the corresponding values from Table 2 for the tension simulations are ~6.2 GPa and ~9.8%. Thus boundary conditions at the end faces influence when the material yields. In simple compression, a dependence of the axial yield stress and the average axial strain at yield on the L/H ratio is also observed. For a given value of L/H, the yield stress in simple tension is higher than that in simple compression. Because of residual stresses in the reference configuration, the difference in the yield stress in simple tension and simple compression cannot be attributed to the Bauschinger effect.

From the elastic constants of Au at 0 K used to find values of parameters in the TB potential, Young's modulus E in the Y-direction is found to equal 46.5 GPa. For the computation of E from results of the MS simulations a representative length L_g was defined around the mid-section of each specimen. A straight line by the least squares method was fit to values of the average axial stress and the average axial strain obtained by taking contributions of atoms inside the length L_g; the slope of the line equals E. Let a equal the inter-atomic spacing in a perfect Au lattice. For $L_g/a < 10$ the value of E varies between 46.8 GPa and

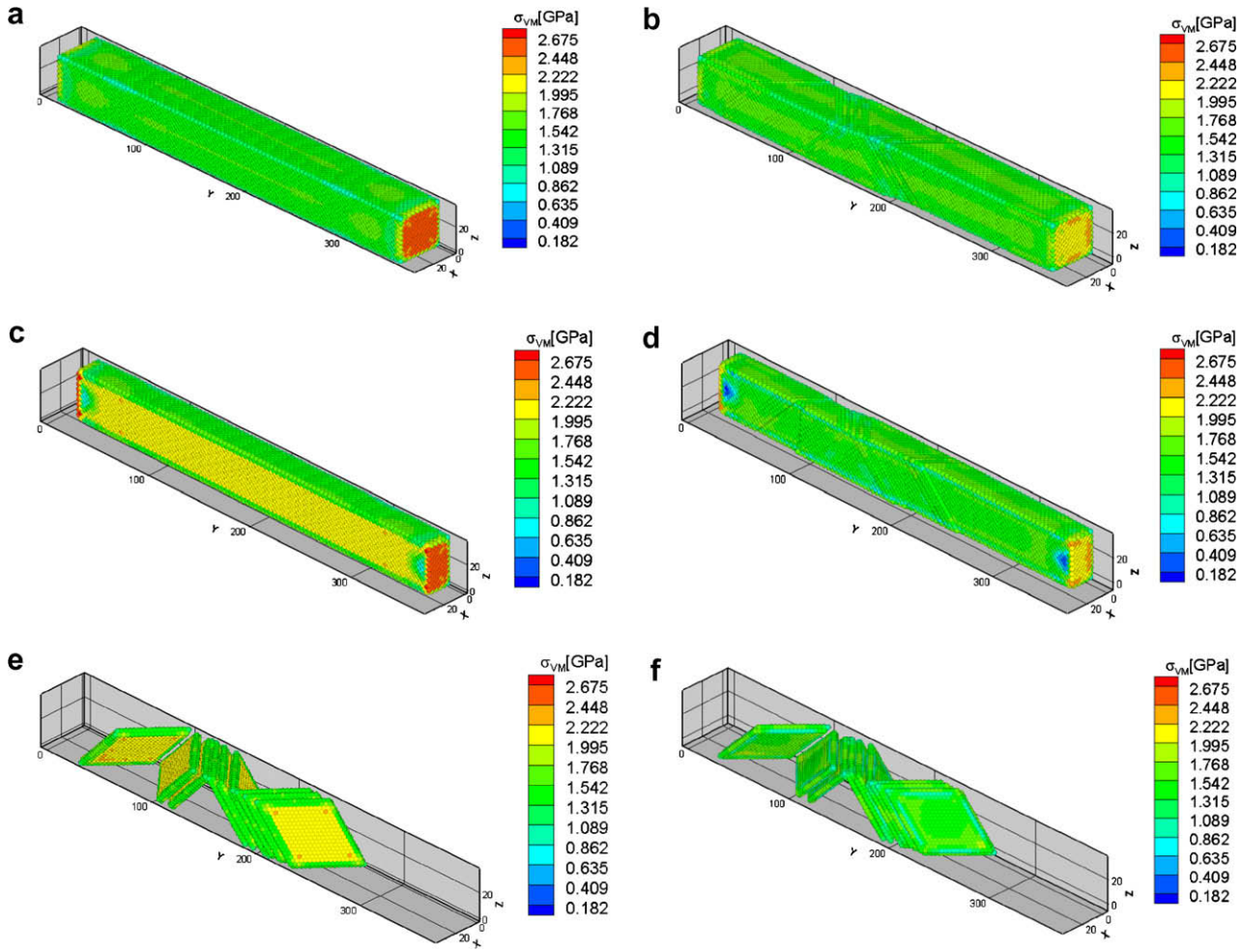

Fig. 11. For simulations of the simple compressive deformations of the specimen with $L/H = 10$, distribution of σ_{VM} stress on (a and b) the bounding surfaces, (c and d) the mid-section, $X = 18$ Å, and (e and f) at points where the minimum eigenvalue of the local Hessian matrix has become negative; for Figs. (a, c and e) $\varepsilon = -5.15\%$; and for (b, d and f) $\varepsilon = -5.16\%$.

47.9 GPa; the difference between the maximum and the minimum values of E is only 2.3%, and the minimum value 46.8 GPa of E differs from the expected value 46.5 GPa by only 0.7%. For $10 < L_g/a < 40$ the value of E equals ~47.1 GPa. Thus it is better to consider a small gage length centered at the middle of the specimen. Boundary effects are reflected in changes of the distribution of inter-atomic forces but their influence along the axial direction goes up to 1 or 1.5 times specimen's width which agrees with Saint–Venant's principle. Poisson's ratio ν was computed from the lateral and the axial strains averaged over atoms in the length L_g. For the specimen having $L/H = 10$, and for $10 < L_g/a < 30$, the computed value 0.478 of ν agrees well with the expected value 0.453 obtained from values of material parameters used to find constants in the TB potential.

5.3. Stress distributions in the specimen

5.3.1. Simple compression

For $L/H = 10$, Figs. 8–12 show, respectively, distributions of σ_{yy}, σ_{xx}, σ_{xy}, σ_{VM} and τ_{max} at $\varepsilon = \varepsilon_{yy}^{yield} = -5.15\%$ and at $\varepsilon = -5.16\%$ that just exceeds ε_{yy}^{yield}. The distribution of σ_{yy} on bounding surfaces in Fig. 8a at $\varepsilon = -5.15\%$ is tensile even though overall deformations are compressive. The maximum value, 0.896 GPa, of the tensile axial stress nearly equals the magnitude, 0.807 GPa, of the compressive axial stress at the specimen centroid. The distribution of σ_{yy} on the bounding surfaces is symmetric about the three centroidal planes. Values of σ_{yy} at points on the edges and at points in the middle of the bounding surface are quite large. At a slightly larger value of the axial strain that just exceeds the axial strain at yield, values of σ_{yy} on the bounding surfaces are nearly uniform, are tensile and equal 1.32 GPa; however, its values are compressive at interior points of the specimen. Values of σ_{yy} at the eight corners and at points on the four edges are not very high as compared to those at the interior points. For a 3D square prismatic continuous body composed of a linear elastic material, one expects at least one component of the Cauchy stress to have very large values at the vertices and at points on the corners.

For $\varepsilon = -5.15\%$, Fig. 8c shows the distribution of σ_{yy} on the mid-section; σ_{yy} is compressive and nearly uniform in

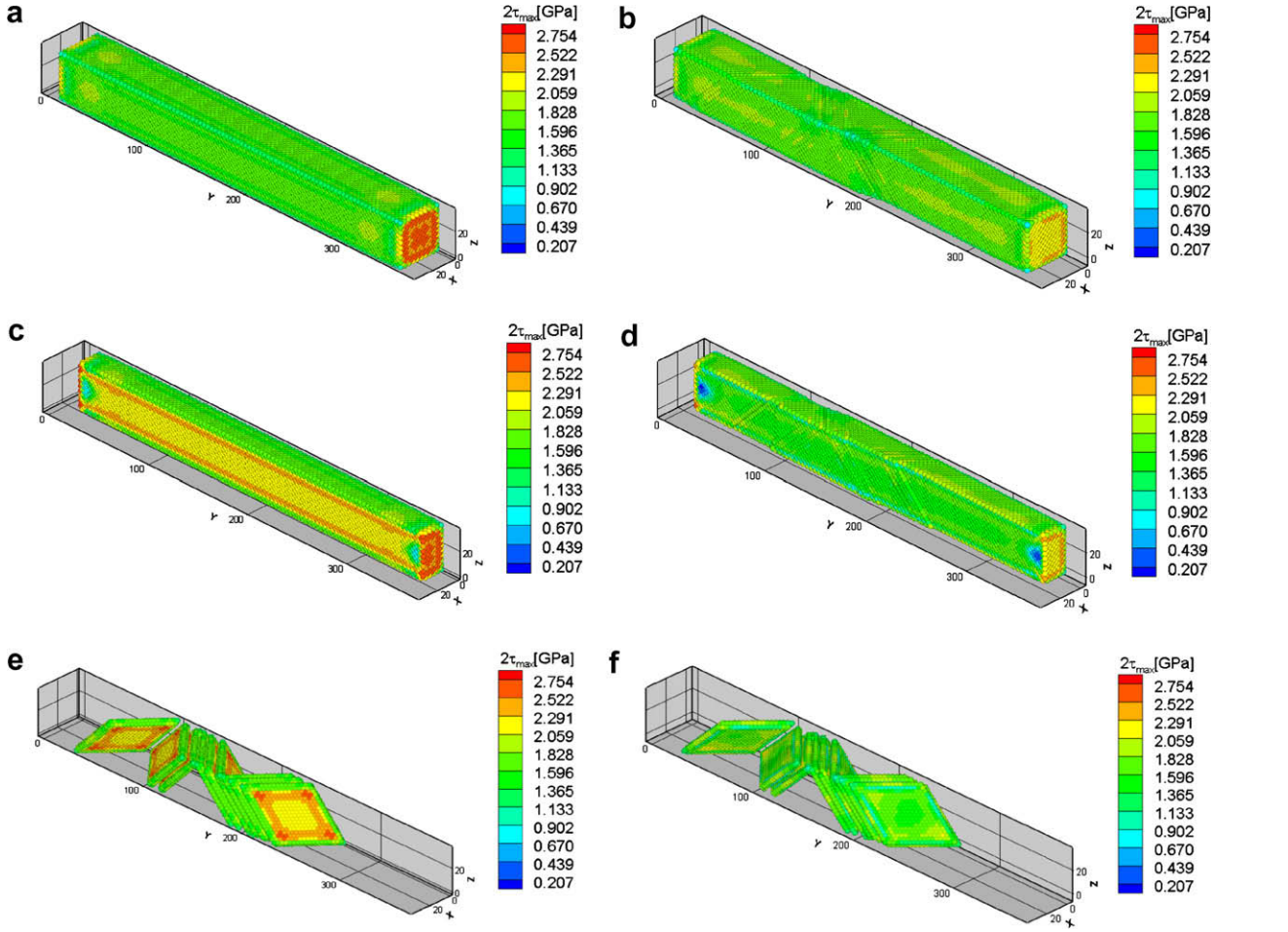

Fig. 12. For simulations of the simple compressive deformations of the specimen with $L/H = 10$, distribution of $2\tau_{max}$ stress on (a and b) the bounding surfaces, (c and d) the mid-section, $X = 18$ Å, and (e and f) at points where the minimum eigenvalue of the local Hessian matrix has become negative; for Figs. (a, c and e) $\varepsilon = -5.15\%$; and for (b, d and f) $\varepsilon = -5.16\%$.

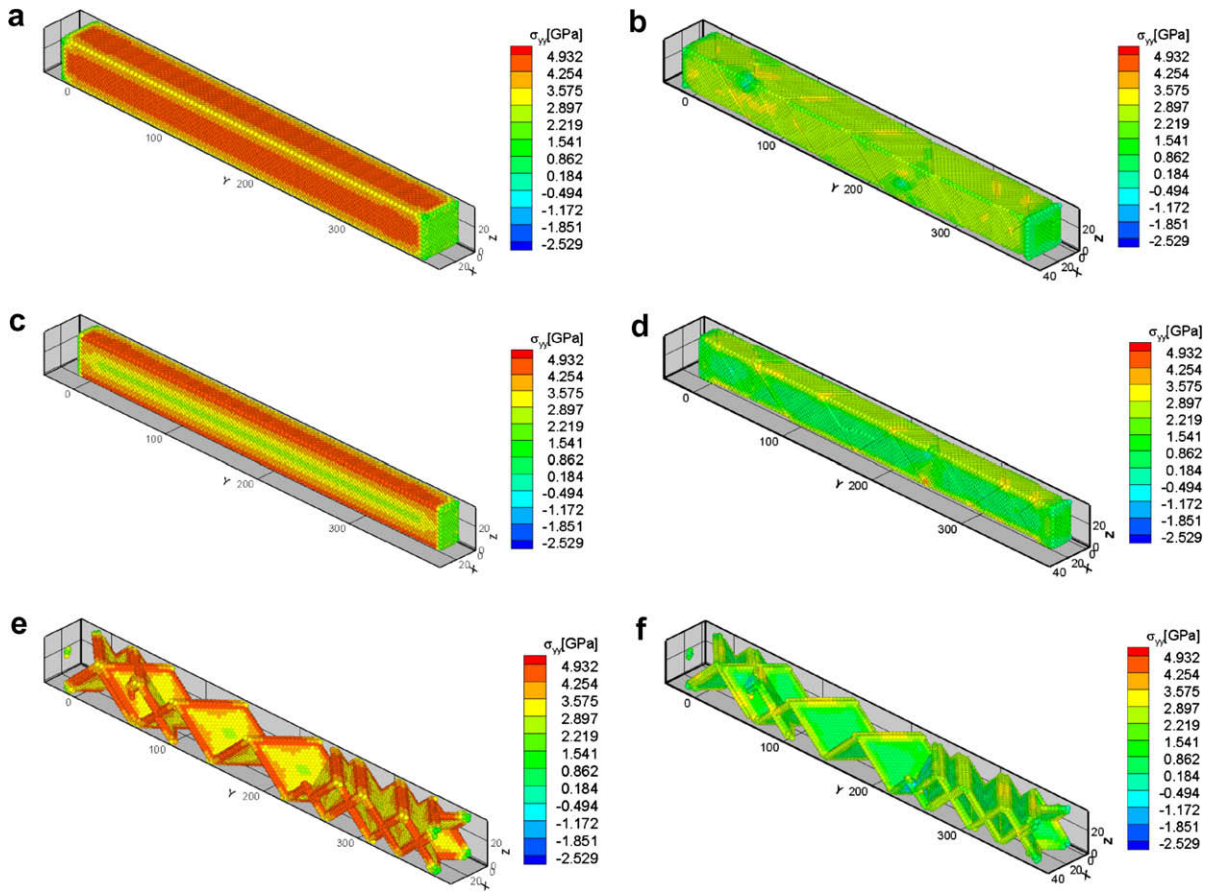

Fig. 13. For simulations of the simple tensile deformations of the specimen with $L/H = 10$, distribution of σ_{yy} component of the local Cauchy stress tensor on (a and b) the bounding surfaces, (c and d) the mid-section, $X = 18$ Å, and (e and f) at points where instabilities have initiated; for Figs. (a, c and e) $\varepsilon = 8.08\%$; and for (b, d and f) $\varepsilon = 8.15\%$.

the interior of the sample with values between -2.51 and -2.94 GPa. Near the free surfaces the stress changes from negative to positive values in a very short distance of $\sim$4 Å. Two groups of atoms having smaller compressive stress than that in atoms at the center of the specimen are symmetrically located at a distance of $\sim L/4$ from each end of the specimen. Close to the end faces, the compressive stress in a small group of atoms forming a dark blue circle in the figure equals -3.36 GPa, which is more than twice the average value of σ_{yy} in the specimen.

In Fig. 8d we have displayed the distribution of σ_{yy} on the mid-section when $\varepsilon = -5.15\%$. The tensile axial stress on the free lateral surface $Z = Z_{max}$ increases from $\sim$0.7 GPa at $\varepsilon = \varepsilon_{yy}^{yield}$ to $\sim$1.3 GPa just after yielding. Thus the onset of yielding does not decrease stresses everywhere. The axial stress at points on the end faces where displacements are prescribed remains essentially unchanged with a small increase in ε from -5.15% to -5.16%. However, at points in the interior of the specimen, the axial stress drops from -2.7 GPa to -1.7 GPa. The size of regions of high compressive stresses close to the edges present in Fig. 8c corresponding to $\varepsilon = \varepsilon_{yy}^{yield}$ is diminished in Fig. 8d but there are still two small groups of atoms with $|\sigma_{yy}| = \sim 1.5$ GPa near the center of the specimen and close to the end faces.

A closer view of the stress level at unstable points after the specimen has yielded is given in Fig. 8e and f. These points correspond to atomic positions where the minimum eigenvalue of the local Hessian matrix is negative. Unstable points are located far from the two end faces and are concentrated near the center of the specimen on planes of high atomic density. At $\varepsilon = \varepsilon_{yy}^{yield}$, in every one of the rhombic forms of unstable atoms, the axial stress is nearly uniform and is ~ -2.7 GPa at the center and changes rapidly from compressive to tensile for atoms close to the free surfaces. For atoms at the center a drop in the stress level to ~ -1.7 GPa is observed after yielding. The reduction in the magnitude of the compressive stress in the interior is accompanied by an increase in the tensile stress at atoms on the traction free bounding surfaces.

Fig. 9 depicts distributions of σ_{xx} on different planes at $\varepsilon = -5.15\%$ and -5.16%. From results plotted in Fig. 9a and those in previous configurations not included here, we conclude that till $\varepsilon = \varepsilon_{yy}^{yield}$ the distribution of σ_{xx} is symmetric with respect to the three centroidal planes, and σ_{xx} at points on the bounding plane, $X = 36$ Å, is negligible

as compared to the maximum value, ~1.9 GPa, of σ_{xx} at other points. The condition of zero traction and hence zero normal stress should be satisfied on this plane. However, the computed values of σ_{xx} on this plane are not exactly zero because it is not perfectly flat in the reference configuration obtained after the minimization of the potential energy.

Fig. 9c shows the distribution of σ_{xx} on the mid-section, $X = 18$ Å. Values of σ_{xx} in the interior of the specimen range from −0.436 to −0.777 GPa; these values are one-fifth of those of σ_{yy} at the same locations. Values of σ_{xx} change along the Z-direction from compressive for atoms in the interior to tensile for atoms on the boundary. The distributions of σ_{xx} in Fig. 9e and f for atoms that have become unstable are very similar for configurations just before and just after the discontinuity in the stress–strain curve. The pattern on each one of the rhombic planes is not uniform but is symmetric with respect to the centroidal axes of the planes. Even though the number of unstable points in the configuration at $\varepsilon = -5.16\%$ is more than that in the configuration at $\varepsilon = -5.15\%$ the general distribution and the magnitude of σ_{xx} remain essentially unchanged.

For $\varepsilon = -5.15\%$ and -5.16% distributions of the shear stress σ_{xy} are depicted in Fig. 10. Values of σ_{xy} are close to zero except at points located on the two end faces of the specimen. These atomic positions with nonzero values of σ_{xy} are located along edges parallel to the Z-axis. The same behavior is observed for distributions of σ_{xz} and σ_{yz} components except that the nonzero values are along edges parallel to the Y- and the X-axes respectively. From Fig. 8e, f, we conclude that even at atoms that have become unstable, values of shear stresses for the present choice of the coordinate planes remain negligible as compared to values of σ_{yy}.

To compare stress levels at different points in the specimen and their relation, if any, with the nucleation of instabilities, values of the von Mises stress and the maximum shear stress were computed. These two quantities are compared with the yield stress of the material in simple tension/compression to possibly formulate a yield criterion in the continuum theory. The distributions of σ_{VM} depicted in Fig. 11a, b shows values ranging from 1.31 to 1.76 GPa at points on the four lateral surfaces. Values around 0.5 GPa before and after the nucleation of instabilities are observed on edges along the Y-axis and at the corners of the specimen. Maximum values of σ_{VM}, ~2.67 GPa, occur on planes where boundary conditions are applied. After the drop in the average axial stress–average axial strain curve, values of σ_{VM} at points on the two end faces vary between 2.0 and 2.4 GPa. The value of σ_{VM} is almost

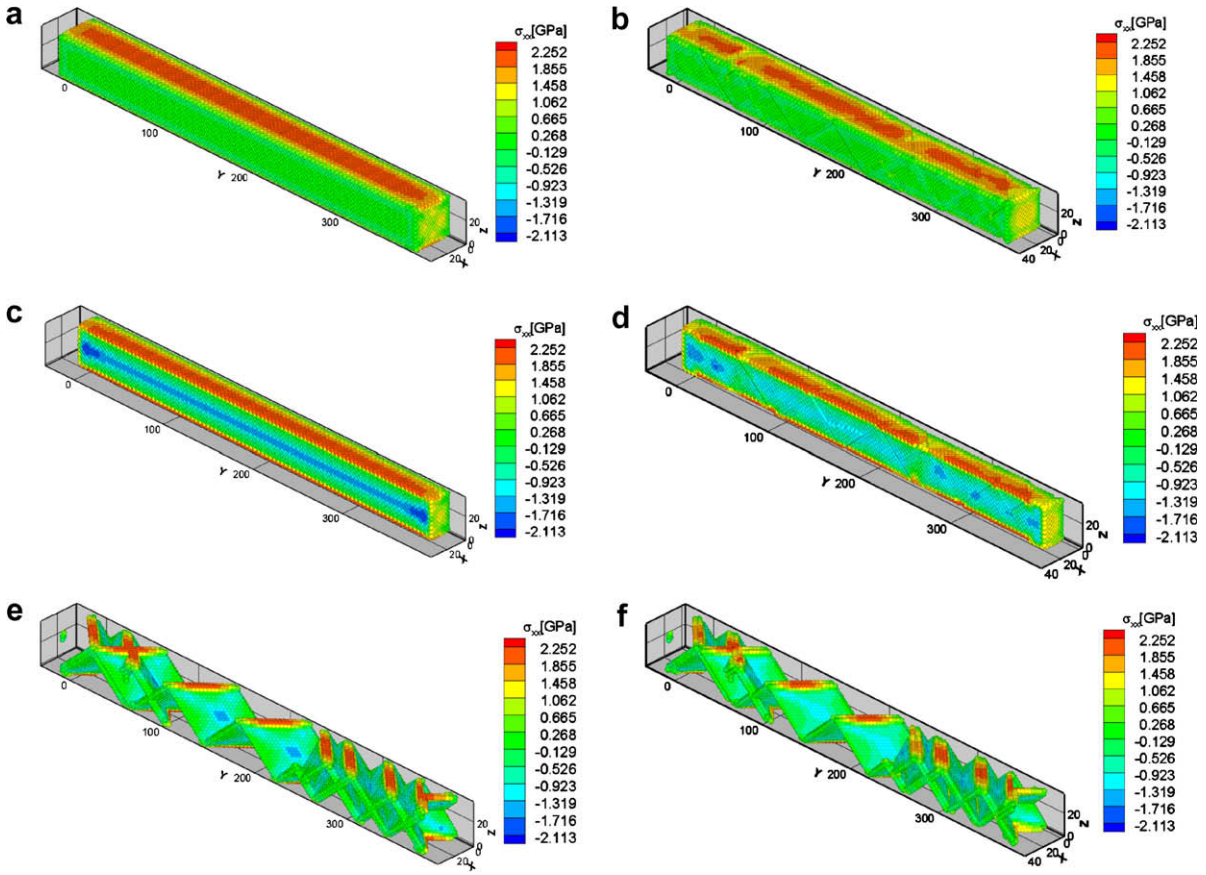

Fig. 14. For simulations of the simple tensile deformations of the specimen with $L/H = 10$, distribution of σ_{xx} component of the local Cauchy stress tensor on (a and b) the bounding surfaces, (c and d) the mid-section, $X = 18$ Å, and (e and f) at points where instabilities have initiated; for Figs. (a, c and e) $\varepsilon = 8.08\%$; and for (b, d and f) $\varepsilon = 8.15\%$.

constant at points in the interior of the specimen prior to the nucleation of instabilities and it ranges from 2.0 to 2.22 GPa except for atoms located close to the end faces. Near the end faces there are groups of atoms having values of σ_{VM} between 0.63 and 1.31 GPa. However, atoms with the same stress level as that in atoms at the center enclose these regions. After the drop in the average axial stress–average axial strain curve, values of σ_{VM} at most points in the interior of the specimen vary between 1.0 and 2.0 GPa. The lowest value, ~0.18 GPa, of σ_{VM} is found at the same group of atoms close to the two end faces as was observed for the configuration just before the nucleation of instabilities.

Of special interest are atoms on four lines parallel to the Y-axis with a high value of σ_{VM} as compared to that at the remaining atoms in the specimen. These lines are located three atomic layers below the lateral free surfaces and atoms on them have a stress level between ~2.22 and ~2.44 GPa. From fringe plots of Fig. 11e and f we see that values of σ_{VM} at points on these lines (orange dots in the planar surfaces) drop from ~2.7 GPa to ~1.3 GPa when $|\varepsilon|$ is increased from 5.15% to 5.16%; after the nucleation of instabilities σ_{VM} at atoms in the interior of the specimen equals ~1.3 GPa. Even though the value of σ_{VM} at atoms on these four lines is higher than that at atoms in the interior of the specimen the difference between the two values is less than the difference between the values of σ_{VM} at atoms in the interior of the specimen and at atoms located on the end surfaces where boundary conditions are applied. We note that none of the atoms on surfaces with prescribed displacements where the highest values of σ_{VM} occur become unstable. Atoms that become unstable are located away from the end faces by at least one-tenth of the specimen length.

Fig. 12a, b depicts, for $\varepsilon = -5.15\%$ and $\varepsilon = -5.16\%$, the distribution of $2\tau_{max}$ in the specimen, i.e., the absolute value of the difference between the minimum and the maximum eigenvalues of the Cauchy stress tensor at each atomic position. The distribution of $2\tau_{max}$ is uniform over the four lateral surfaces with values ranging from 1.1 to 2.0 GPa. The value of $2\tau_{max}$ peaks at ~2.75 GPa for atoms located on the two end faces of the specimen. Fig. 12c shows, prior to the nucleation of instabilities, values of $2\tau_{max}$ between 2.0 and 2.3 GPa for atoms around the centroidal line parallel to the Y-axis. From the fringe plots on the mid-section $X = 18$ Å reported in Fig. 12c we notice two lines parallel to the Y-axis on which $2\tau_{max}$ is the same as that on the two end faces. These atoms of high shear stress are located on a square band that surrounds the interior of the specimen. The shear stress at atoms located $3a/2$

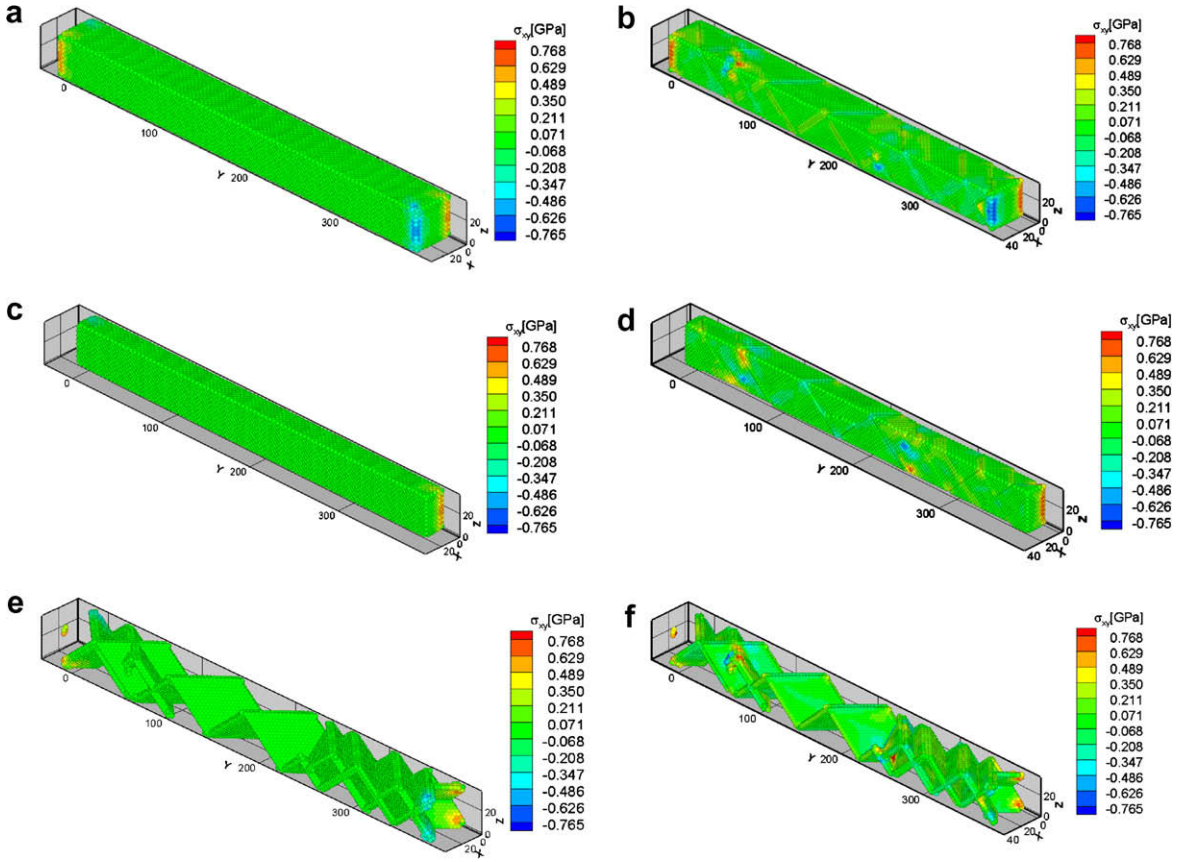

Fig. 15. For simulations of the simple tensile deformations of the specimen with $L/H = 10$, distribution of σ_{xy} component of the local Cauchy stress tensor on (a and b) the bounding surfaces, (c and d) the mid-section, $X = 18$ Å, and (e and f) at points where instabilities have initiated; for Figs. (a, c and e) $\varepsilon = 8.08\%$; and for (b, d and f) $\varepsilon = 8.15\%$.

from the free surface (e.g., yellow regions close to the lateral surfaces) nearly equals that at atoms at the center of the specimen.

Fig. 12e, f depicts the distribution of $2\tau_{max}$ at atoms just before and immediately after their becoming unstable. After the nucleation of instabilities $2\tau_{max}$ drops from ~2.75 to ~1.8 GPa for points that had maximum values of $2\tau_{max}$ prior to their becoming unstable and from ~2.1 to ~1.13 GPa for points at the specimen center. As was also observed in the distributions of σ_{yy} and σ_{VM}, stresses at most atoms in the system decrease after the nucleation of instabilities.

Contrary to the distribution of the maximum values of σ_{VM} prior to the occurrence of instabilities, the distribution of $2\tau_{max}$ shows that the maximum values of shear stresses occur in regions where instabilities nucleate. Values of $2\tau_{max}$ at points on the traction free surfaces are nearly one-quarter of the maximum values at atoms just below the free surfaces.

5.3.2. Simple tension

For $L/H = 10$, Fig. 13 exhibits the distribution of σ_{yy} in configurations corresponding to $\varepsilon = 8.08\%$ and $\varepsilon = 8.15\%$. In contrast to the distribution of σ_{yy} for simple compression, the distribution of σ_{yy} in Fig. 13a for simple tension on the lateral surfaces is uniform along the Y-direction, and $\sigma_{yy} = \sim 4.93$ GPa. Smaller values, ~3.2 GPa, of σ_{yy} occur at points near the edges. At points near the two end faces σ_{yy} equals one-fifth of its maximum value at points on the lateral surfaces. Subsequent to the initiation of instabilities, the distribution of σ_{yy} displayed in Fig. 13b is non-uniform and σ_{yy} on the lateral surfaces has dropped from ~4.9 GPa to ~3 GPa.

Fig. 13c depicts the distribution of σ_{yy} on the mid-section, $X = 18$ Å, when $\varepsilon = 8.08\%$. The magnitude of σ_{yy} increases from ~0.5 GPa at the centroid of the specimen to ~4.93 GPa at points on the free lateral surfaces. An initially compressive stress of ~ -1.5 GPa at points on the centroidal axis in the reference configuration changes to tensile stress with increasing axial deformations. The magnitude of the in-plane tensile stress at atoms on the traction free lateral surfaces increases from ~1.8 GPa at $\varepsilon = 0\%$ to ~4.5 GPa at $\varepsilon = 8.08\%$. Fringe plots of σ_{yy} exhibited in Fig. 13d reveal that at points around the center of the specimen, σ_{yy} is relaxed from ~2.8 GPa before the nucleation of instabilities to ~1.4 GPa just after the nucleation of instabilities; for atoms on traction free surfaces this reduction in σ_{yy} is from ~4.5 GPa to ~2.6 GPa.

From the distributions of σ_{yy} on planes of atoms that become unstable during the next load step, shown in Fig. 13f, it is clear that the axial stress increases from ~2.8 GPa at the center to ~4.5 GPa at points on the free surfaces. This is different from that in the simple compressive deformations where a high gradient in σ_{yy} occurs at

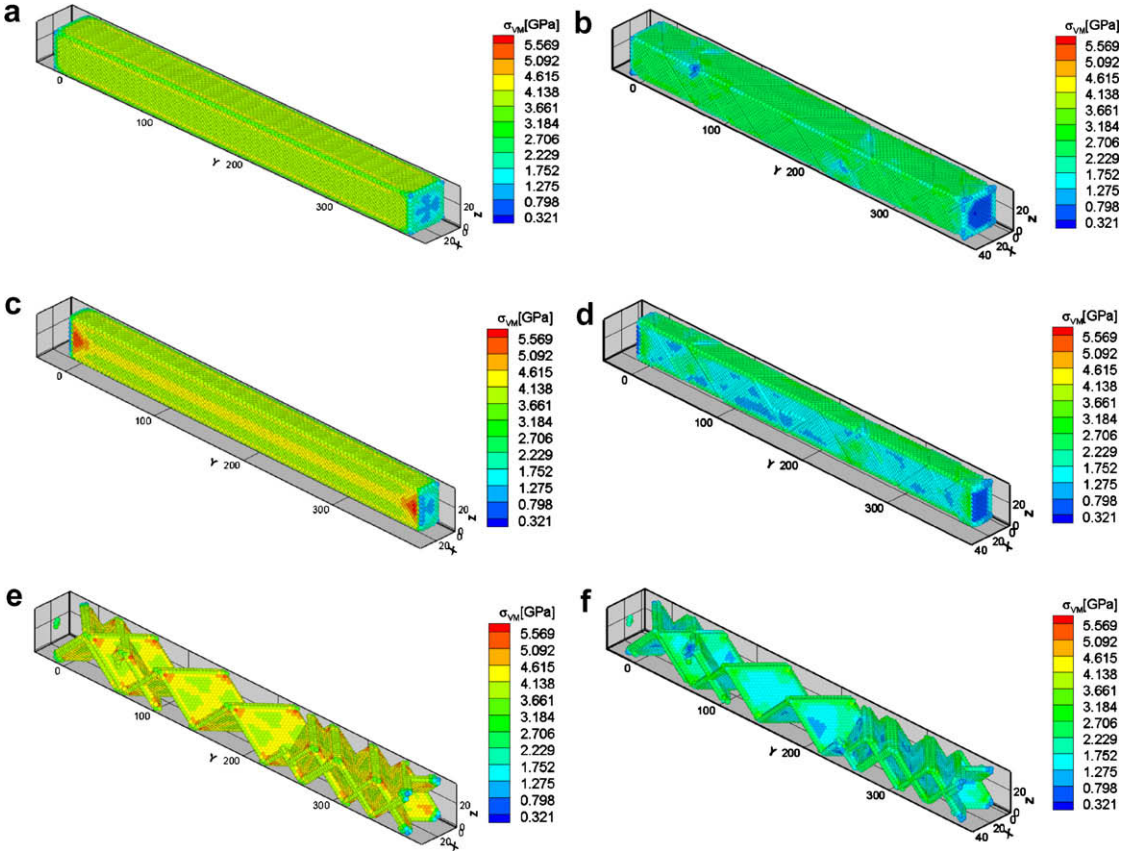

Fig. 16. For simulations of the simple tensile deformations of the specimen with $L/H = 10$, distribution of σ_{VM} on (a and b) the bounding surfaces, (c and d) the mid-section, $X = 18$ Å, and (e and f) at points where instabilities have initiated; for Figs. (a, c and e) $\varepsilon = 8.08\%$; and for (b, d and f) $\varepsilon = 8.15\%$.

points close to the lateral traction free surfaces due to the difference in the signs of the axial stress (compressive at the center and tensile at points on the free surfaces). During the nucleation of instabilities at these atoms σ_{yy} drops by ~40%; e.g. compare fringe plots in Fig. 13e, f.

The distribution of σ_{xx} depicted in Fig. 14a is similar to the one observed in simple compressive deformations. On lateral surfaces, $X = 0$, 36 Å, the value of σ_{xx} is negligible, consistent with the boundary conditions of null traction on these surfaces. However, at lateral surfaces, $Z = 0$, 36 Å, $\sigma_{xx} \approx 2.25$ GPa. From the fringe plots of Fig. 14c it can be noticed that σ_{xx} at the specimen centroid is compressive and its magnitude equals that of the tensile stress at points on traction free surfaces, $Z = 0$, 36 Å. After the occurrence of local instabilities the symmetry in the distribution of σ_{xx} is lost but the magnitude of σ_{xx} remains essentially unchanged even at atoms that have become unstable (see Fig. 14c, f). At a point in the specimen σ_{zz} and σ_{xx} are equal till $\varepsilon = 8.05\%$; subsequently no major qualitative changes occur in σ_{zz} and σ_{xx}.

As for simple compressive deformations values of σ_{xy} are negligibly small till $\varepsilon = \varepsilon_{yy}^{yield}$, i.e., 8.08%, except at atoms along the four vertical edges parallel to the Z-axis (cf. Fig. 15a, c). After the occurrence of local instabilities the magnitude of σ_{xy} reaches a maximum of ~0.76 GPa at some points located close to the bounding surfaces.

The distribution of σ_{VM} on the bounding surfaces is depicted in Fig. 16a, b; it is essentially uniform on these surfaces prior to the nucleation of instabilities with values ranging from ~2.22 to ~4.61 GPa. Fringe plots of Fig. 16c show that on the mid-section, $X = 18$ Å, values of σ_{VM} at points near the end faces of the specimen are higher than those at points on its lateral surfaces. Two groups of atoms, starting with the third layer from the end faces, have the maximum value ~5.57 GPa of σ_{VM}; it rapidly decreases to ~4.3 GPa, and stays at that value on atoms near the longitudinal centroidal axis of the specimen. At points near the center, values of σ_{VM} vary between ~4.3 GPa and ~3.8 GPa along the Z- and the X-axes. A high gradient in the values of σ_{VM} is found at points close to the free lateral surfaces while that at points near the center is moderate. The distribution of σ_{VM} at points where instabilities have initiated, depicted in Fig. 14e, shows the presence of four lines of atoms with $\sigma_{VM} = \sim 5.57$ GPa, which is nearly the same as that at points close to the edges of the mid-section. At these points, after the nucleation of instabilities, the σ_{VM} drops to ~2 GPa; a similar drop in the stress level occurs at all atoms in the rhombic planes of unstable atoms shown in Fig. 16f. We note that none of the

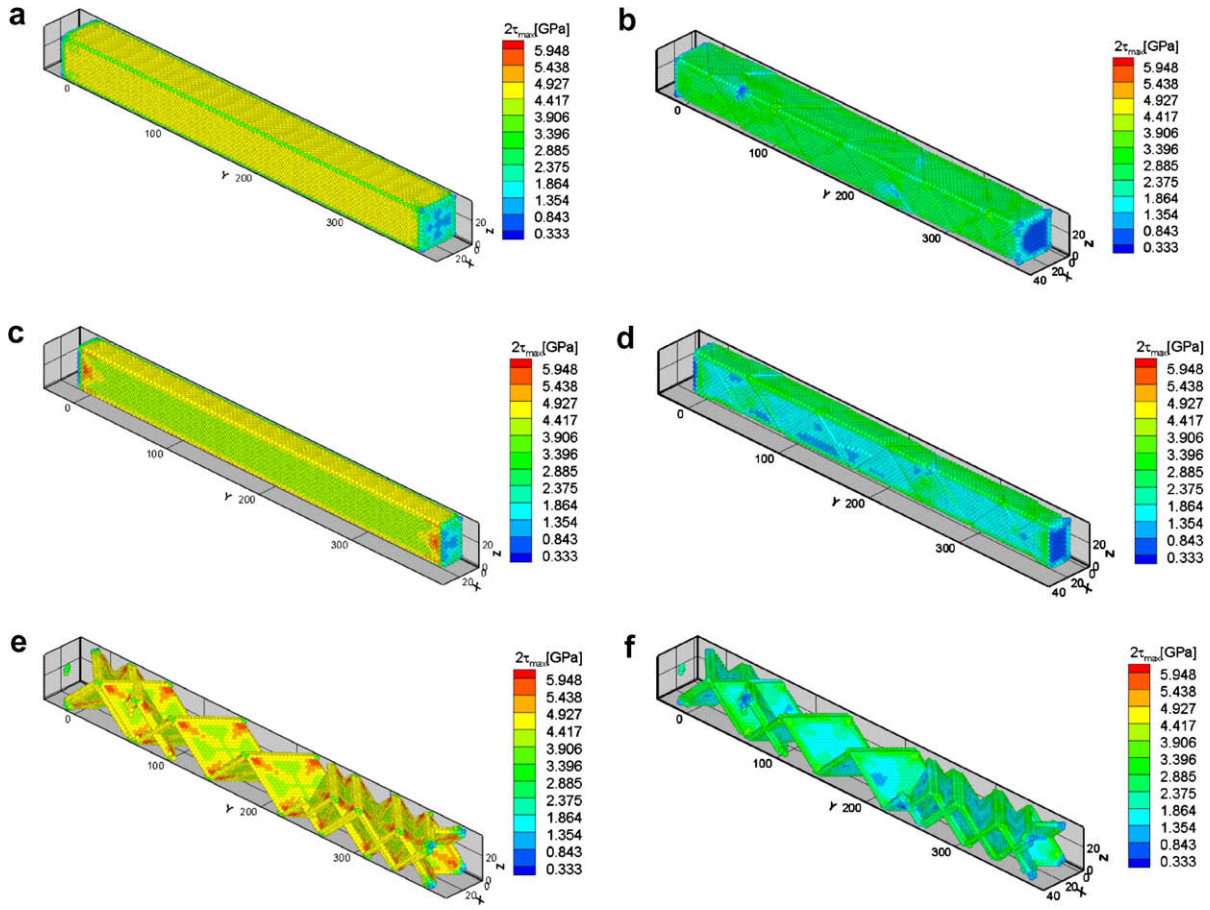

Fig. 17. For simulations of the simple tensile deformations on the specimen with $L/H = 10$, distribution of $2\tau_{max}$ on (a and b) the bounding surfaces, (c and d) the mid-section, $X = 18$ Å, and (e and f) at points where instabilities have initiated; for Figs. (a, c and e) $\varepsilon = 8.08\%$; and for (b, d and f) $\varepsilon = 8.15\%$.

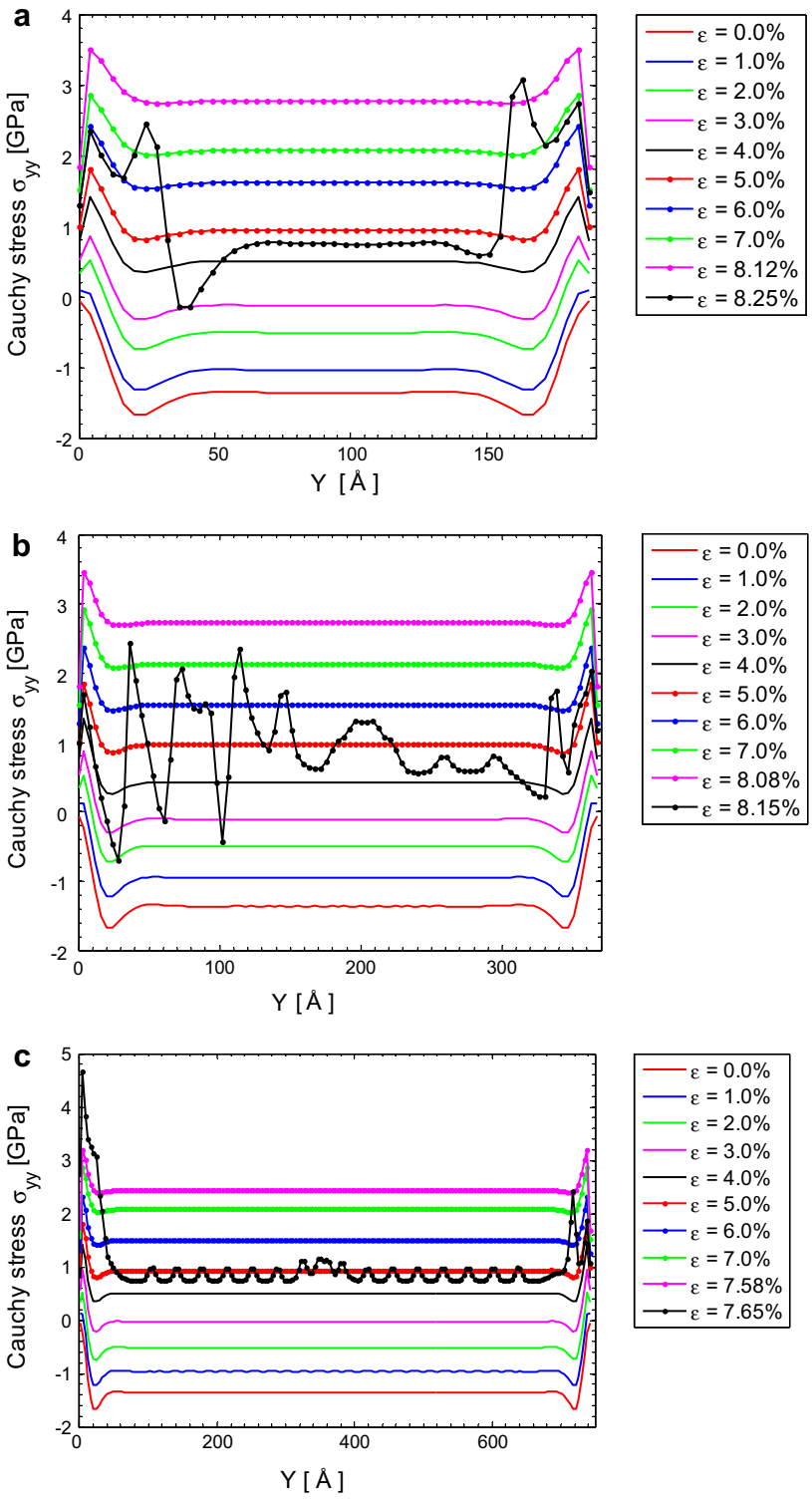

Fig. 18. For simulations of the simple tensile deformations, variation with the average axial strain ε of σ_{yy} component of the local Cauchy stress tensor along the centroidal axis; (a) $L/H = 5$, (b) $L/H = 10$, and (c) $L/H = 20$.

atoms with high values of σ_{VM} located at the end faces becomes unstable.

The distributions of $2\tau_{max}$ in Fig. 17a–f are similar to those of σ_{VM} in Fig. 16a–f. For establishing a relation, if any, between the stress level and the nucleation of instabilities, we note that the maximum values of $2\tau_{max}$ and σ_{VM} at $\varepsilon = \varepsilon_{yy}^{yield}$ at points that have become unstable are different for simple tension and simple compression. For simple

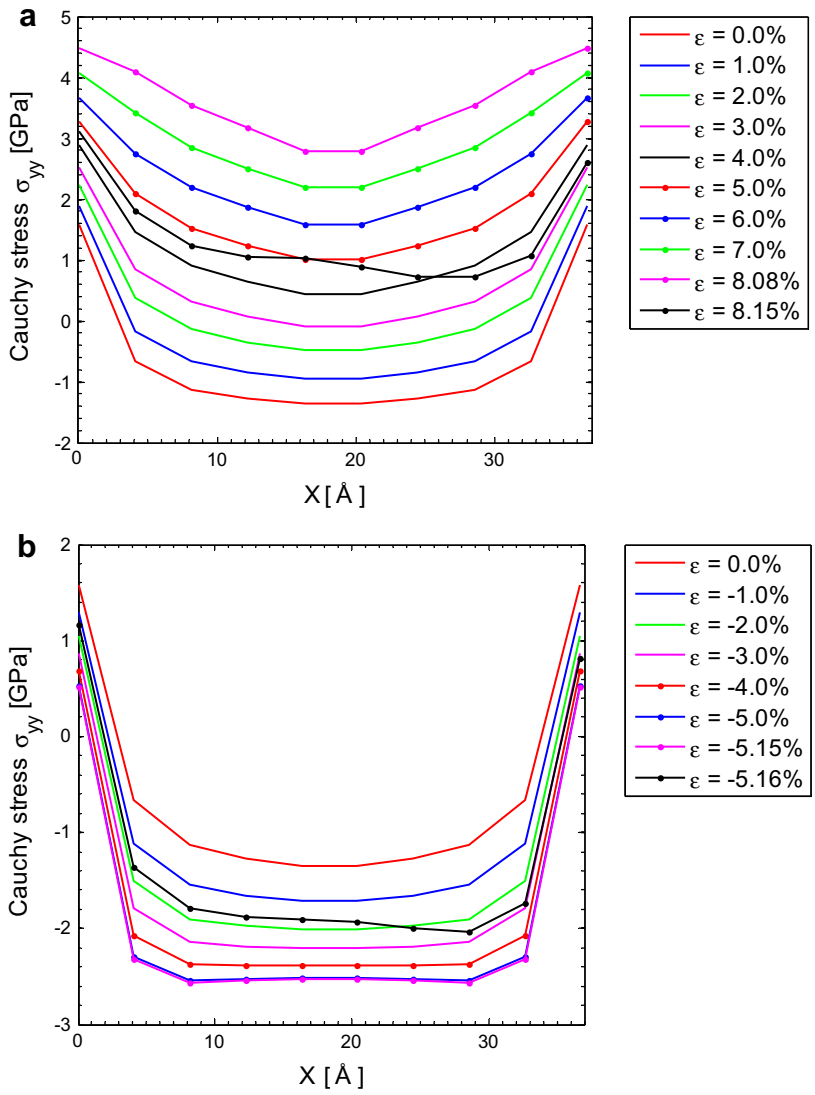

Fig. 19. For $L/H = 10$, variation with the axial strain ε of the σ_{yy} component of the local Cauchy stress tensor along the X-centroidal line; (a) simple tension and (b) simple compression.

compression, the maximum values of $2\tau_{max}$ and σ_{VM} are 2.75 and 2.33 GPa, respectively. For simple tension, $2\tau_{max}$ and σ_{VM} equal 5.95 and 5.57 GPa, respectively. There is a difference of ~100% between these values, showing that for this specific case

$$(\tau_{\max})_{tension} =\sim 2(\tau_{\max})_{compression} \quad \text{and}$$
$$(\sigma_{VM})_{tension} =\sim 2(\sigma_{VM})_{compression}.$$

5.4. Effect of the aspect ratio L/H

5.4.1. Simple tension

For simple tension and $L/H = 5$, 10 and 20, Fig. 18a–c exhibits distributions of σ_{yy} on the centroidal axis at various values of the average axial strain ε. For $\varepsilon < \varepsilon_{yy}^{yield}$, σ_{yy} changes rapidly at points close to the end faces, $Y = Y_{min}$ and $Y = Y_{max}$, and saturates to a constant value at the center. At $\varepsilon = 0$, i.e., the reference configuration, σ_{yy} is close to zero at points near the two end faces but it is compressive at other points on the centroidal axis; the maximum magnitude of $\sigma_{yy} \sim 1.7$ GPa is at points whose distance from the end faces equals 20 Å. At points near the center of the specimen $\sigma_{yy} \sim -1.2$ GPa for the three L/H values. The σ_{yy} at a point increases with an increase in the deformation. At $\varepsilon = \sim 1\%$, the stress at points near the end faces becomes tensile. At $\varepsilon = 4\%$, σ_{yy} is positive (tensile) at all points on the centroidal axis. Until $\varepsilon = \varepsilon_{yy}^{yield}$, the qualitative and the quantitative evolutions of σ_{yy} are the same for $L/H = 5$, 10 and 20. The material yields at $\varepsilon = \sim 8\%$ with a stress level of $\sigma_{yy} = \sim 2.8$ GPa at the center for $L/H = 5$ and 10 and $\sigma_{yy} = \sim 2.4$ GPa for $L/H = 20$.

The black curves in Fig. 18a–c give the distribution of σ_{yy} on the centroidal axis for ε slightly greater than ε_{yy}^{yield}.

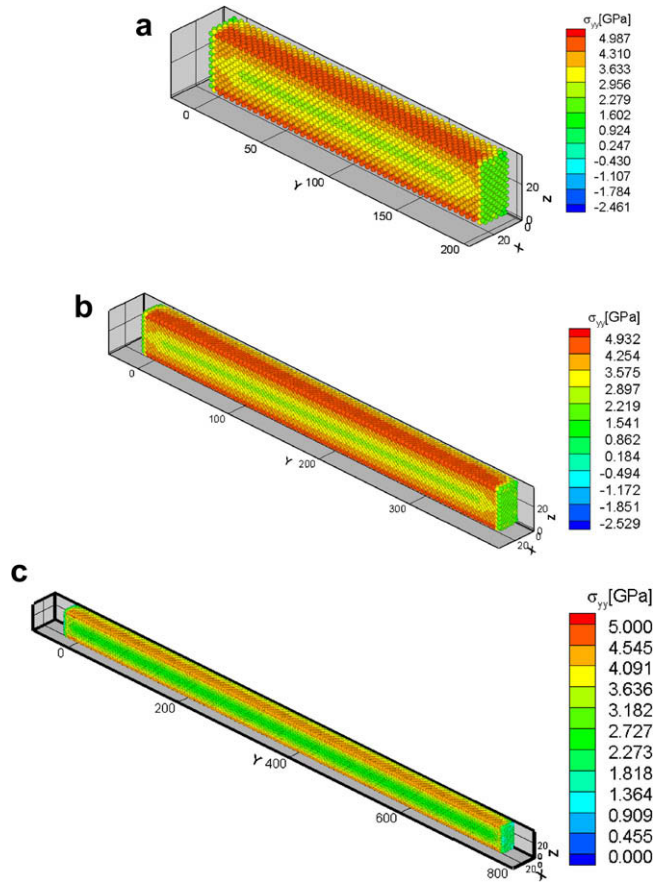

Fig. 20. For simulations of the simple tensile deformations, distribution of the local Cauchy stress tensor component σ_{yy} on the mid-section $X = H/2$ at $\varepsilon = \varepsilon_{yy}^{yield}$; (a) $L/H = 5$, (b) $L/H = 10$, and (c) $L/H = 20$.

After the nucleation of local instabilities in the specimen, the distribution of σ_{yy} becomes asymmetric about the plane $Y = L/2$; σ_{yy} decreases by different amounts at various points on the centroidal axis and its distribution depends upon the value of L/H. This asymmetry could be due to atoms on the end face $Y = Y_{min}$ being restrained from moving in the Y-direction but those on the end face $Y = Y_{max}$ moved axially. We recall that the distribution of unstable points in the specimen is not the same for all L/H ratios.

Fig. 19a shows, for $L/H = 10$, the variation of σ_{yy} on the centroidal line $Y = L/2$, $Z = H/2$. At $\varepsilon = 0$, σ_{yy} is compressive at points away from the lateral traction free surfaces. As the axial deformation increases σ_{yy} in the cross-section becomes positive. At $\varepsilon = \sim 3\%$, $\sigma_{yy} > 0$ everywhere on the centroidal line. For $\varepsilon < \varepsilon_{yy}^{yield}$, the distribution of σ_{yy} on the centroidal line is symmetric about $X = H/2$. The variation of σ_{yy} on the centroidal axis $Y = L/2$, $X = H/2$ is similar to that on the centroidal axis $Y = L/2$, $Z = H/2$.

Fig. 20a–c depicts distributions on the mid-surface $X = H/2$ of σ_{yy} at $\varepsilon = \varepsilon_{yy}^{yield}$ for $L/H = 5$, 10 and 20 respectively. The three distributions are qualitatively similar in that the maximum tensile stress ~5 GPa occurs at points on the lateral surfaces, and the minimum tensile stress ~2.8 GPa at points on and near the centroidal axis.

Fig. 21a and b depicts, for four different values of L/H, distributions of σ_{xx} and σ_{yy} on the centroidal axis for the four specimens in configurations corresponding to $\varepsilon = 0$ and $\varepsilon = \varepsilon_{yy}^{yield}$. Results have been plotted in the reference configuration and the horizontal axis has been normalized by the length of the specimen in the reference configuration. From Fig. 21a we see that the distribution of σ_{yy} on the centroidal axis is similar for the four specimens. At $\varepsilon = 0$, σ_{yy} equals zero at atoms close to the end faces and is compressive at other points. Assuming that the surface stress σ_{yy} is proportional to the curvature of the surface, the plots of Fig. 21a imply that the curvature of the bounding surface in the reference configuration varies smoothly as one goes inwards from the end faces.

With an increase in the axial tensile strain, σ_{yy} switches from compressive to tensile at points on the centroidal axis. However, σ_{xx} at points on the centroidal axis stays compressive with its magnitude increasing with an increase in ε. For $L/H = 20$, at the specimen centroid, $\sigma_{xx} = -0.7$ GPa, $\sigma_{yy} = -1.35$ GPa when $\varepsilon = 0$, and $\sigma_{xx} = -1.5$ GPa, $\sigma_{yy} = 2.5$ GPa when $\varepsilon = \varepsilon_{yy}^{yield}$, whereas, initially, $\sigma_{xx} = \sigma_{zz} \approx 0.5\ \sigma_{yy}$ at the specimen centroid, at yielding $|\sigma_{xx}| = |\sigma_{zz}| \approx 0.6\ \sigma_{yy}$. Note that in the reference configuration the three normal stresses are compressive but in the deformed configuration corresponding to $\varepsilon = \varepsilon_{yy}^{yield}$, σ_{xx} and σ_{zz} are compressive but σ_{yy} is tensile.

5.4.2. Simple compression

At different strain levels for $L/H = 5$, 10 and 20 Fig. 22a–c shows, respectively, distributions of σ_{yy} along the centroidal line parallel to the Y-axis. For different values of the axial strain ε, distributions of σ_{yy} on the centroidal line parallel to the Y-axis are qualitatively and quantitatively similar to each other for $L/H = 5$, 10 and 20. The magnitude of the compressive stress at a point continuously increases with an increase in the axial deformation up to $\varepsilon = \varepsilon_{yy}^{yield}$. For $L/H = 5$, at $\varepsilon = \sim$-3%, a concavity in the distribution of σ_{yy} at the center of the specimen is observed. This small concavity, not observed for $L/H = 10$ and 20, becomes more pronounced with increasing compressive deformation. After $|\varepsilon| > \sim 5\%$, $|\sigma_{yy}|$ at points on the centroidal line for the specimen with $L/H = 5$ does not increase appreciably; in Fig. 22a curves for $|\varepsilon| \geqslant \sim 6\%$ almost overlap each other until the yield point is reached. At $|\varepsilon|$ just greater than $|\varepsilon_{yy}^{yield}|$ the variation of σ_{yy} with Y depends upon the specimen size.

Fig. 19b shows, for $L/H = 10$, the variation of σ_{yy} along the centroidal line parallel to the X-axis. The initially tensile stresses on the free surfaces $X = X_{min}$ and $X = X_{max}$ decrease and the compressive stresses in the interior increase monotonically till $\varepsilon = -5.15\%$. As σ_{yy} in the specimen approaches the yield stress the rate of change of σ_{yy} with ε decreases at the specimen centroid. However, gradients of stresses at points close to the free surfaces remain essentially unchanged. This differs substantially from that in tensile deformations (see Fig. 19a).

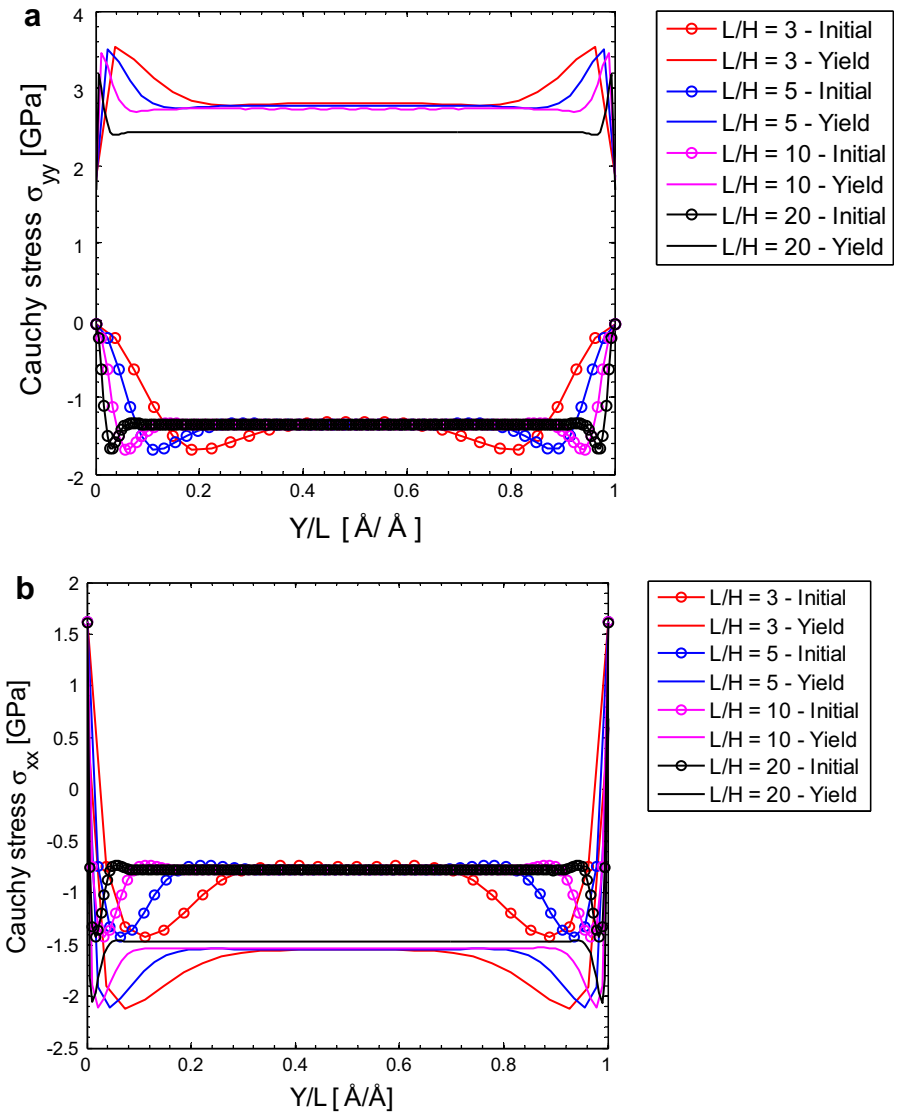

Fig. 21. For simple tensile deformations at $\varepsilon = 0$ and $\varepsilon = \varepsilon_{yy}^{yield}$, variation of the local Cauchy stresses σ_{yy} and σ_{xx} along the Y-centroidal line; (a) σ_{yy} and (b) σ_{xx}.

Fig. 23a–c depicts the distribution at $\varepsilon = \varepsilon_{yy}^{yield}$ of σ_{yy} on the mid-section $X = H/2$ of specimens with $L/H = 5$, 10 and 20 respectively. The distribution in the specimen of the axial stress at the yield point for $L/H = 5$ is quite different from that in specimens with $L/H = 10$ and 20. At the yield point $|\sigma_{yy}|$ at points on the lateral traction free surfaces varies from ~0.005 to ~0.444 GPa; only small groups of atoms on the lateral traction free surfaces located at ~30 Å from the two loaded end faces have higher tensile stress σ_{yy} than that at atoms at the center of the lateral surfaces. These high values of the tensile stress on the lateral surface are observed in those cross-sections that have high values of compressive stresses at interior points. For $L/H = 10$ and $L/H = 20$ atoms on lateral surfaces with high positive values of σ_{yy} are spread along the length of the specimen. At points far from the two loaded end faces, the distribution in the specimen of σ_{yy} is nearly uniform. On a cross-section the stress σ_{yy} changes gradually from negative at the centroid to positive at the free surface.

In Fig. 24 at $\varepsilon = 0$ and $\varepsilon = \varepsilon_{yy}^{yield}$ the variations of σ_{xx} and σ_{yy} along the Y-centroidal line have been plotted for specimens with $L/H = 3$, 5, 10 and 20. The distributions of σ_{xx} and σ_{yy} in the reference configuration are similar for the four specimens. The maximum compressive stresses occur at the same relative locations and their values become uniform on the central four-tenths of the specimen length. However, at the yield point, the stress distribution depends upon L/H. For $L/H = 3$ and 5 the stress distribution on the central portion of the specimen length is non-uniform but for $L/H = 10$ and 20 it is uniform. Values of σ_{xx} and σ_{yy} in the central four-tenths of the specimen length depend upon L/H; their magnitudes are the maximum for $L/H = 3$ and the minimum for $L/H = 20$. At $\varepsilon = \varepsilon_{yy}^{yield}$, $\sigma_{xx} \approx 0.46\ \sigma_{yy}$, $0.6\ \sigma_{yy}$, $0.85\ \sigma_{yy}$ and $0.9\ \sigma_{yy}$ for $L/H = 20$,

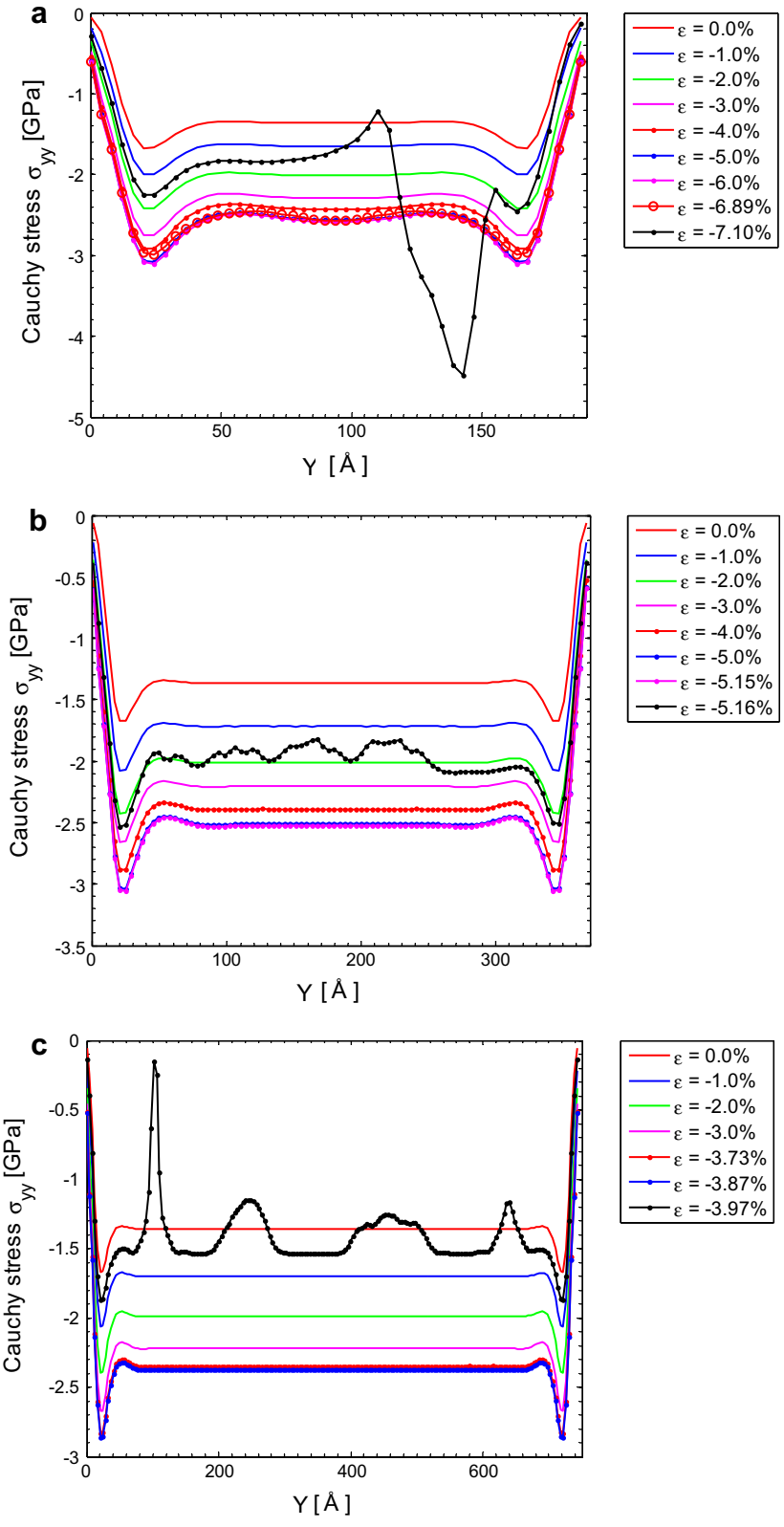

Fig. 22. For simulation of the simple compressive deformations, variation with the average axial strain ε of σ_{yy} component of the local Cauchy stress tensor along the centroidal axis; (a) $L/H = 5$, (b) $L/H = 10$, and (c) $L/H = 20$.

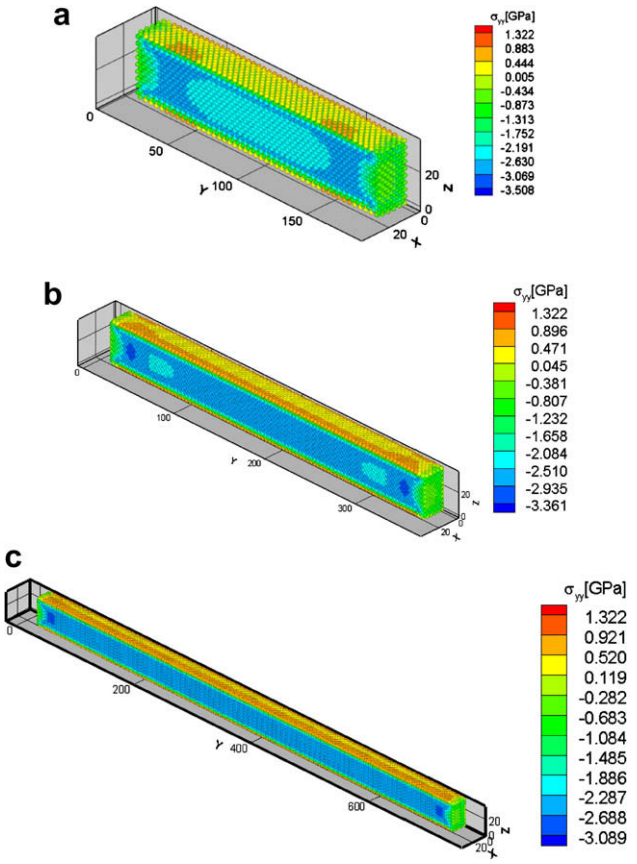

Fig. 23. For simulations of the simple compressive deformations, distribution of the σ_{yy} component of the local Cauchy stress tensor on the mid-section $X = H/2$ at $\varepsilon = \varepsilon_{yy}^{yield}$; (a) $L/H = 5$, (b) $L/H = 10$, and (c) $L/H = 20$.

10, 5, and 3, respectively, whereas at $\varepsilon = 0$, $\sigma_{xx} \approx 0.5\ \sigma_{yy}$ for each one of the four values of L/H.

5.5. Comparison of the maximum shear and the von Mises stresses at points where instabilities have initiated

5.5.1. Simple compression

For points where instabilities have initiated just after $\varepsilon = \varepsilon_{yy}^{yield}$, i.e., points identified by negative eigenvalues of $\boldsymbol{H}^{(i)}$, stresses in the configuration for $\varepsilon = \varepsilon_{yy}^{yield}$ have been computed. For $L/H = 5$, 10 and 20, Fig. 25a–c depicts, respectively, distributions of $2\tau_{max}$ on unstable points. Large values, ~2.5 GPa, of τ_{max} at unstable points are observed on atoms three layers below the lateral free surfaces. These atoms are located near the edges of the specimen (corners of the rhombic shape of unstable atoms) for the three L/H ratios. As the average axial strain increases the number of these atoms increases around the corners of the specimen (see red arrows in Fig. 25). Even though there are differences among the average axial yield stresses for the three specimens, the maximum shear stress at yield is about the same (see Table 4). The maximum value of the average axial yield stress is for the specimen with $L/H = 5$. It is clear from the results exhibited in Fig. 25a that large values of $2\tau_{max}$ occur at points on the third and the fourth layers of atoms located parallel to the lateral traction free surfaces. Points in the interior experience higher shear stresses as the strain level increases; this is evidenced by the increase in the number of atoms in the orange band surrounding atoms with high values of $2\tau_{max}$. It is important to note that atoms with the maximum value of the shear stress are not located on the traction free surfaces but beneath them.

For $L/H = 5$, 10 and 20, Fig. 26a–c depicts distributions of σ_{VM} at unstable points. As for the distributions of $2\tau_{max}$ the highest values of the von Mises stress occur at points near the four corners of the specimens that are on the third layer below the traction free surface. The maximum value, ~2.23 GPa, of σ_{VM} is almost the same for specimens with $L/H = 5$ and $L/H = 10$. The maximum value, ~2.1 GPa, for $L/H = 20$, is slightly less than that for the other two specimens.

5.5.2. Simple tension

The distributions of $2\tau_{max}$ at $\varepsilon = \varepsilon_{yy}^{yield}$ for simulations of the simple tensile deformations of specimens with $L/H = 5$, 10 and 20 are depicted in Fig. 27a–c. As for simple compressive deformations, atoms with high values of the maximum shear stress are near the edges of the specimen (the corners of the rhombic plane of unstable atoms). Points with high values of $2\tau_{max}$ are located right beneath the lateral free surfaces. In contrast to results for simple compression, the pattern for the distribution of stresses is the same for the three specimens. The maximum value, ~5.9 GPa, of $2\tau_{max}$ is also the same for the three specimens.

As the average axial stress increases, high values of $2\tau_{max}$ occur at atoms located along the diagonals of the cross-section near the center of the specimen. This distribution contrasts with the one observed in simple compression where interior atoms having high stress levels form a closed rectangular band. Values of $2\tau_{max}$ decrease from 5.9 GPa at points on the edges, to 4.5, 4.3 and 3.9 GPa at the centroid of the specimen for $L/H = 5$, 10 and 20, respectively.

For $L/H = 5$, 10 and 20 and $\varepsilon = \varepsilon_{yy}^{yield}$, Fig. 28a–c depicts distributions of σ_{VM} on unstable atoms. The distribution of σ_{VM} is similar to that for $2\tau_{max}$ with large values at atoms localized in clusters near the corners of the rhombic planes of unstable atoms. The minimum value of σ_{VM} among values at unstable points does not occur at the atom at the specimen centroid.

From the distributions of σ_{VM} and $2\tau_{max}$ for simulations of the simple tensile deformations we note that the maximum stress levels are reached at the same locations in the three specimens; these results are summarized in Table 5.

6. Remarks

The mechanical behavior of an atomic system depends upon the temperature. Parameters for empirical potentials like the TB and the EAM are fitted via elastic constants, lattice parameter and equilibrium conditions at 0 K. For performing simulations at a temperature other than 0 K,

one needs to use a thermostat and keep either the volume or the pressure constant that brings another variable into the problem. Furthermore, integration of the governing equations with respect to time requires time steps of the order of pico- or femto-seconds, making simulations for reasonable axial strains computationally very expensive.

At temperatures other than 0 K, it is not clear whether or not the computation of the stress tensor should contain contributions from the linear momentum terms. Furthermore, as recently mentioned by Subramaniyan and Sun [34], some empirical potentials are not temperature-compensated. These authors heated a model atomistic solid and computed the stress tensor under different boundary conditions using the Irving–Kirkwood expression [24], which contains potential and kinetic terms, and concluded that the term containing the kinetic part cannot be neglected from the calculation as suggested by Zhou [14]. Hoover et al. [22] have computed the stress tensor of an elastic rotating disk and a system of particles under gravitational forces. They compared their MD results at different temperatures with the analytical results and obtained almost a perfect match. In addition, the authors emphasized that the stress tensor is the negative of the pressure tensor, the co-rotating momentum flux. These results evince that kinetic terms play a role in the computation of stresses at finite temperature but various authors interpret these quantities differently.

Whereas we have used here the TB potential, Jiang and Batra [35] used the EAM potential and the software LAMMS to study axial compression of an Au nanowire. Since the LAMMS is a highly optimized software developed over several years and our in-house software has not been

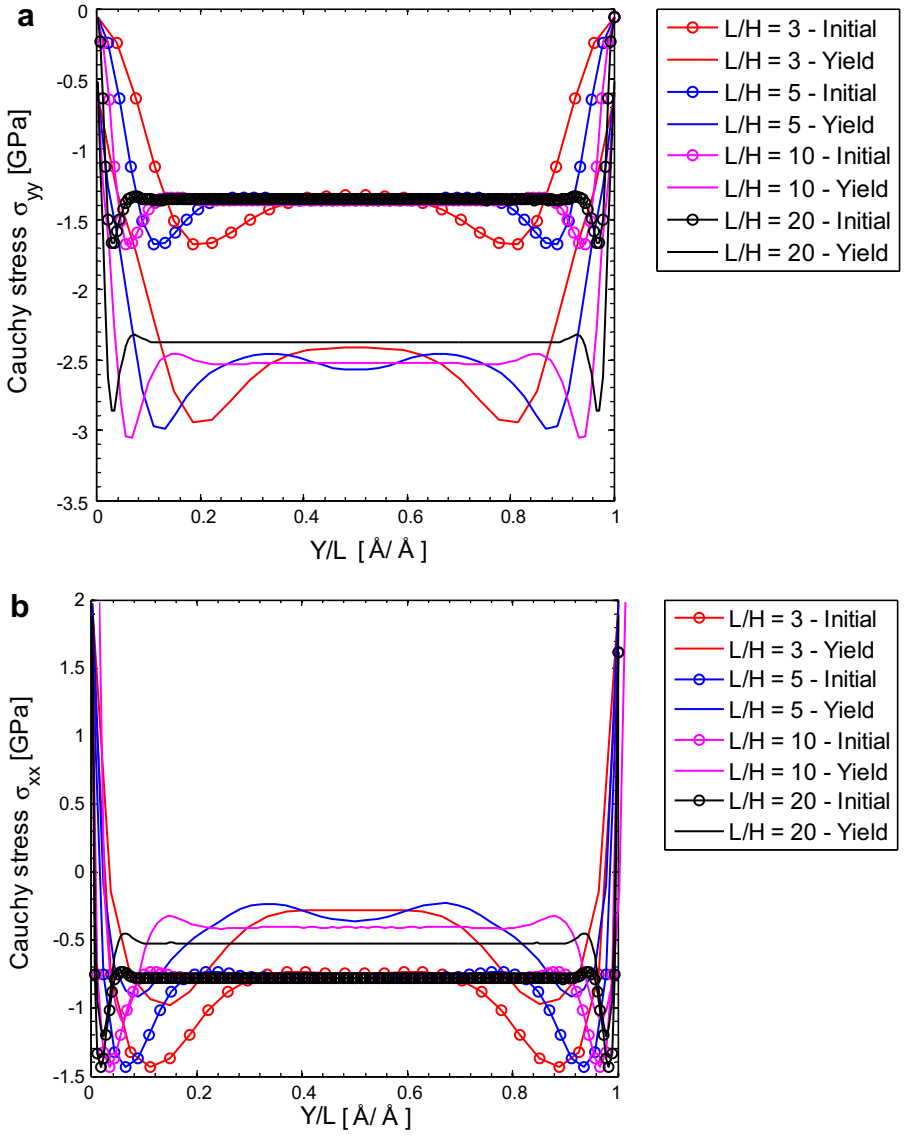

Fig. 24. For simple compressive deformations at $\varepsilon = 0$ and $\varepsilon = \varepsilon_{yy}^{yield}$, variation of the local Cauchy stresses σ_{yy} and σ_{xx} along the Y-centroidal line; (a) σ_{yy} and (b) σ_{xx}.

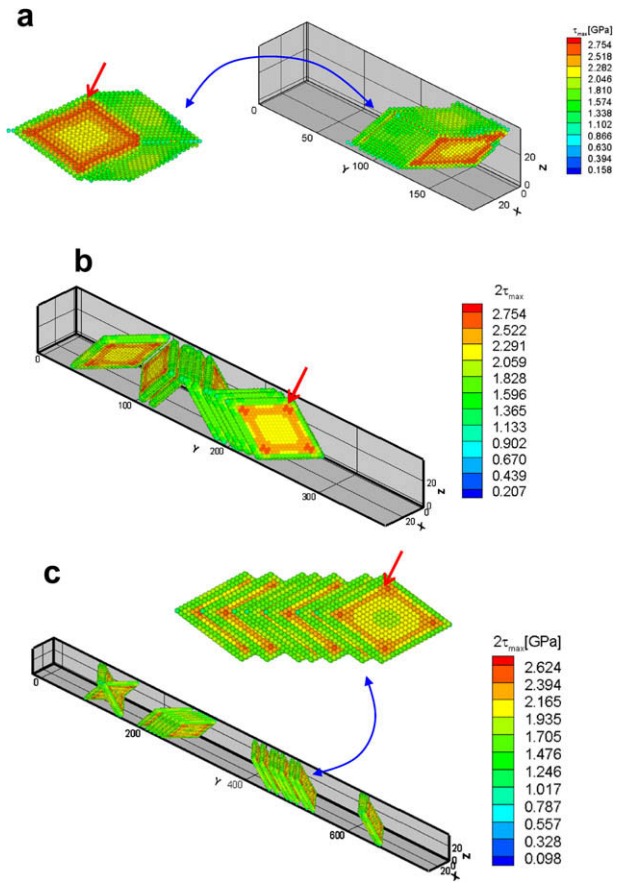

Fig. 25. For simulations of the simple compressive deformations, the distribution of $2\tau_{max}$ at the unstable points when $\varepsilon = \varepsilon_{yy}^{yield}$; (a) $L/H = 5$, (b) $L/H = 10$, and (c) $L/H = 20$. Red arrows indicate points with high stress values. Values of σ_{yy}, σ_{VM} and $2\tau_{max}$ at these points are summarized in Table 4. The blue arrows indicate sections for which an expanded view is provided.

optimized, it is unfair to compare the computational performance of the two software. Leaving the detailed comparison of results from the two potentials for a future study, we note that the two sets of results are different. We note that Pu et al. [36] used three semiempirical potentials, namely, Vorter and Chen's [37] EAM potential, the glue model potential of Ercolessi et al. [38], and the TB potential. They compared results of MD simulations for a tension test on an Au cluster composed of 256 atoms using the three potentials. The accuracy of a potential was determined by comparing predictions of the potential energy in the relaxed configuration and of the ultimate force at the breaking point with results obtained by using the density functional theory (DFT), which were taken as the reference values. The force at the breaking point for an atomic chain of Au atoms was found experimentally by Rubio–Bollinger et al. [39] to be 1.5 ± 0.3 nN. Predictions from the TB potential were found to agree well with the DFT results and the experimental data. The EAM and the glue model potentials overestimated the value of the potential energy of the systems in the initial configuration (no external load applied) and also showed the initial shape of the specimen not agreeing with that obtained through the DFT calculations. It was concluded that the EAM and the glue model potentials are not adequate to describe the energetics of systems with a large number of under-coordinated atoms.

Sen and Buehler [40] have used the Rice–Peierls model to study the initiation of dislocations from the tip of a semi-infinite crack in a thin strip. The inter-atomic interactions were defined by the Morse and the harmonic potentials. They found the existence of intrinsic length scales that depend only on material parameters and the particular geometry. These characteristic length scales separate regimes of no dislocation activity, partial dislocation plasticity, and complete dislocation plasticity at a crack tip in ductile metals. In our work there is no a priori defect or crack introduced in the nano-specimens and dislocations originate when deformations become unstable.

7. Conclusions

We have used molecular statics (MS) simulations to study axial tension/compression and simple axial tension/compression of prismatic gold nanorods of square cross-section with the tight-binding potential with the goal of delineating stress distributions in the specimen. For triaxial deformations of the specimen, we have also compared Cauchy stresses computed with Hardy's method from results of the MS simulations with those found by assuming that the material is hyperelastic whose strain energy is derived from the tight-binding potential and the Cauchy–Born rule. Conclusions from this work are summarized below:

- For isochoric triaxial deformations, variations with the average axial strain of components of the average Cauchy stress tensor and the strain energy computed from MS simulations agree well with those derived from the

Table 4
For specimens with different L/H ratios deformed in simple compression, maximum values at $\varepsilon = \varepsilon_{yy}^{yield}$ of σ_{yy}, σ_{VM} and $2\tau_{max}$ for unstable atoms and the corresponding values for atoms on the centroidal axis. Points with the maximum values are indicated by red arrows in Figs. 23 and 24.

L/H	Maximum values			Maximum values at points on the centroidal line			$(\sigma_{yy})_{average}$ (GPa)
	σ_{yy} (GPa)	σ_{VM} (GPa)	$2\tau_{max}$ (GPa)	σ_{yy} (GPa)	σ_{VM} (GPa)	$2\tau_{max}$ (GPa)	
5	−2.772	2.276	2.555	−2.537	2.212	2.341	−1.810
10	−2.789	2.601	2.601	−2.533	2.087	2.131	−1.671
20	−2.584	2.097	2.422	−2.371	1.850	1.862	−1.387

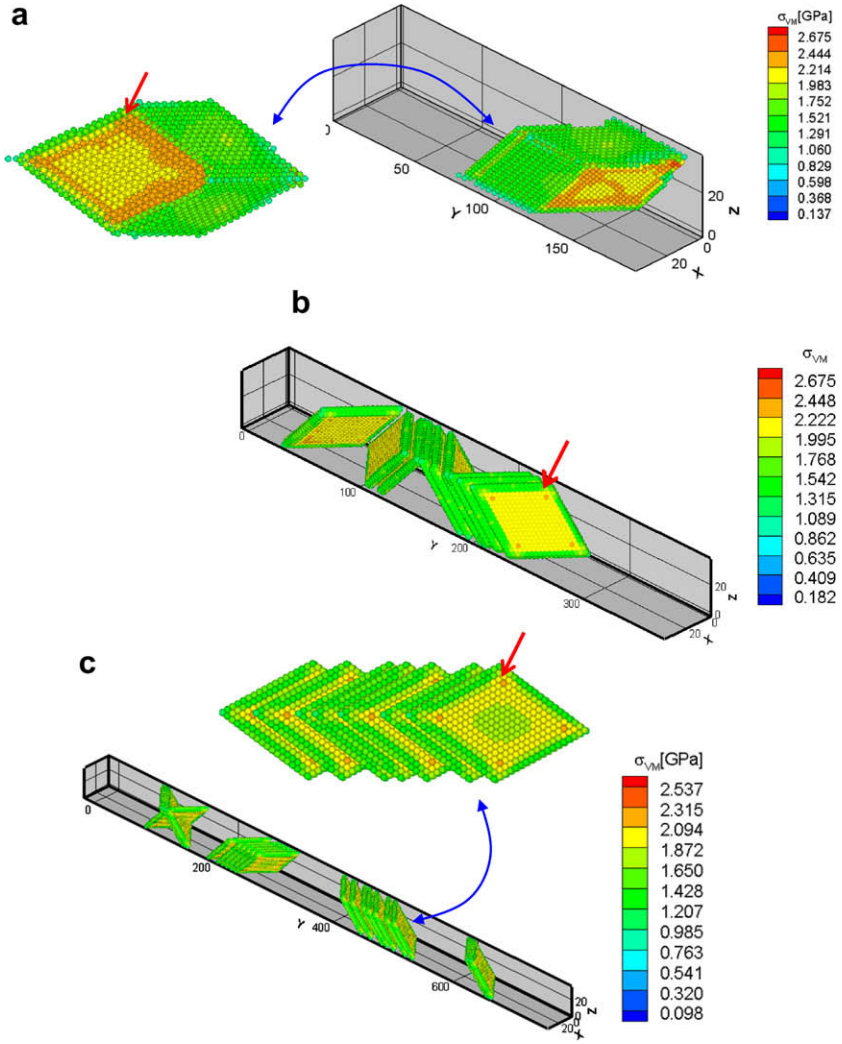

Fig. 26. For simulations of the simple compressive deformations, the distribution of σ_{VM} on the unstable points when $\varepsilon = \varepsilon_{yy}^{yield}$; (a) $L/H = 5$, (b) $L/H = 10$, and (c) $L/H = 20$. Red arrows indicate points with high stress values. Values of σ_{yy}, σ_{VM} and $2\tau_{max}$ at these points are summarized in Table 4. The blue arrows indicate sections for which an expanded view is provided.

analytical expressions obtained by assuming that the body's response is hyperelastic and the strain energy density can be derived from the MS potential by using the Cauchy–Born rule.

- Stresses within the specimen are distributed non-uniformly in the unloaded reference configuration of the minimum potential energy. The global equations of equilibrium are satisfied, and the local equilibrium equations (vanishing of the divergence of the Cauchy stress tensor) are also satisfied everywhere except at points on the specimen edges.
- Large values of the von Mises stress, σ_{VM}, and the maximum shear stress, τ_{max}, occur on atoms located beneath the traction free surfaces, and at atoms in the interior that have become unstable. The places where high values of $2\tau_{max}$ occur prior to the onset of global instability (or yielding) are distributed very differently in simple tension and simple compression. For simple tension these high values are found in a thin axial layer extending to three atomic spaces from the traction free surface whereas for simple compression these zones form squares around the center of the specimen that grow as the external load increases. The number of layers forming this square zone increases with the decrease in specimen's length.
- Except for simple tensile deformations, values of the von Mises stress and the maximum shear stress at specimen's yielding depend upon the specimen size and boundary conditions prescribed on the bounding surfaces.
- The distributions of local stresses on the centroidal lines are essentially independent of the specimen aspect ratio. However, during compressive deformations, the distribution of stresses on the axial centroidal line at yield form a wave-like pattern whose amplitude decreases as specimen's length increases. The correlation, if any, between these wave patterns and instabilities is left for future study.

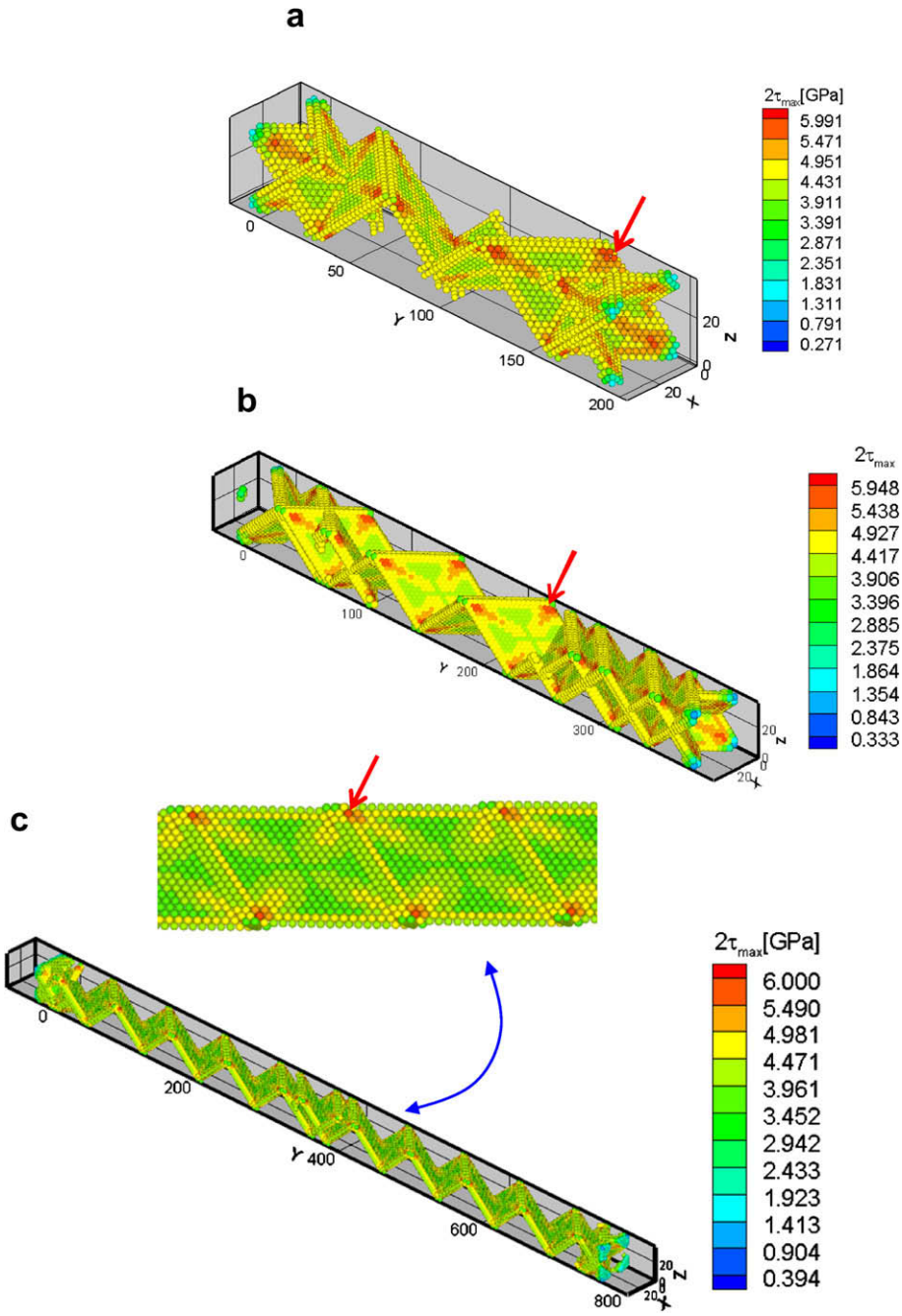

Fig. 27. For simulations of the simple tensile deformations, distribution of $2\tau_{max}$ on unstable points when $\varepsilon = \varepsilon_{yy}^{yield}$; (a) $L/H = 5$, (b) $L/H = 10$, and (c) $L/H = 20$. Red arrows indicate points with high stress values. Values of σ_{yy}, σ_{VM} and $2\tau_{max}$ at these points are summarized in Table 5. The blue arrows indicate sections for which an expanded view is provided.

Table 5
For specimens with different L/H ratios deformed in simple tension, maximum values at $\varepsilon = \varepsilon_{yy}^{yield}$ of σ_{yy}, σ_{VM} and $2\tau_{max}$ for unstable atoms and the corresponding values for atoms on the centroidal axis. Points with the maximum values are indicated by red arrows in Figs. 25 and 26.

L/H	Maximum values			Maximum values at points on the centroidal line			$(\sigma_{yy})_{average}$ (GPa)
	σ_{yy} (GPa)	σ_{VM} (GPa)	$2\tau_{max}$ (GPa)	σ_{yy} (GPa)	σ_{VM} (GPa)	$2\tau_{max}$ (GPa)	
5	4.627	5.204	5.959	2.930	4.322	4.500	4.996
10	4.579	5.155	5.905	2.839	4.285	4.295	4.990
20	4.281	4.865	5.586	2.436	3.907	3.907	4.618

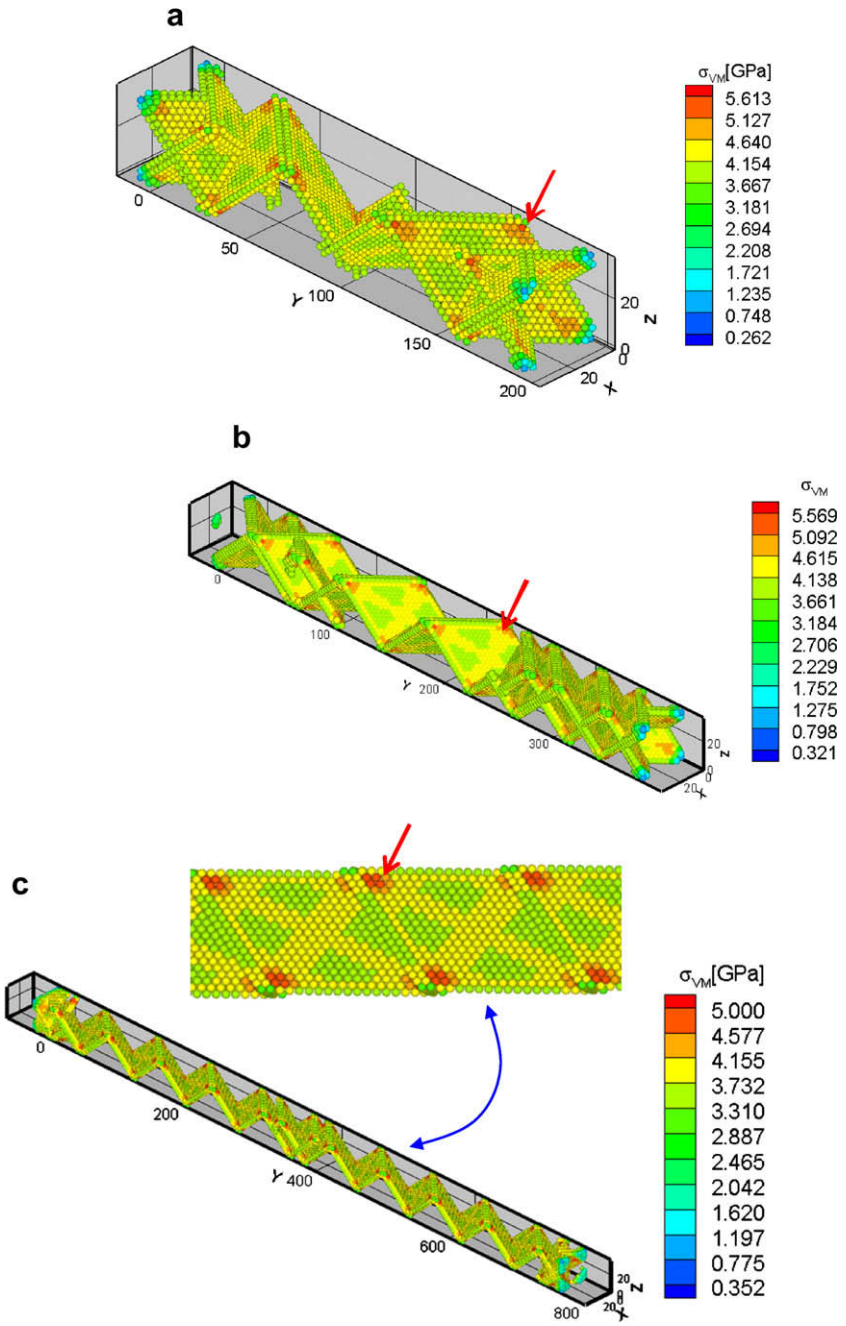

Fig. 28. For simulations of the simple tensile deformations, distribution of σ_{VM} on unstable points when $\varepsilon = \varepsilon_{yy}^{yield}$; (a) $L/H = 5$, (b) $L/H = 10$, and (c) $L/H = 20$. Red arrows indicate points with high stress values. Values of σ_{yy}, σ_{VM} and $2\tau_{max}$ at these points are summarized in Table 5. The blue arrows indicate sections for which an expanded view is provided.

Acknowledgements

This work was partially supported by the ONR Grant N00014-06-1-0567 to Virginia Polytechnic Institute and State University with Dr. Y.D.S. Rajapakse as the program manager, Virginia Tech's Institute of Critical Technologies and Sciences, the COLCIENCIAS – LASPAU scholarship, and the Universidad del Norte in Barranquilla, Colombia. Views expressed herein are those of the authors, and neither of the funding agencies nor of their institutions.

References

[1] Diao J, Gall K, Dunn ML. J Mech Phys Solids 2004;52:1935–62.
[2] Diao J, Gall K, Dunn ML, Zimmerman JA. Acta Mater 2006;54:643–53.
[3] Baskes MI. Phys Rev B 1992;46(5):2727–42.
[4] Gall K, Diao J, Dunn ML. Nano Lett 2004;4(12):2431–6.
[5] Liu Y, van der Giessen E, Needleman A. Int J Solids Struct 2007;44:1719–32.
[6] Miller RE, Rodney D. J Mech Phys Solids 2008;56:1203–23.
[7] Zhang W, Wang T, Chen X. J Appl Phys 2008;103:123527.
[8] Cleri F, Rosato V. Phys Rev B 1993;48(1):22–33.

[9] Hardy RJ. J Chem Phys 1981;76:622–8.
[10] Zhang GM, Batra RC. Comput Mech 2004;34:137–46.
[11] Ericksen JL. Math Mech Solids 2008;13:199–220.
[12] Tsai DH. J Chem Phys 1979;70(3):1375–82.
[13] Lutsko JF. J Appl Phys 1988;64(3):1152–4.
[14] Zhou M. Proc Roy Soc Lond A 2003;459:2347–62.
[15] Ogata S, Li J, Hirosaki N, Shibutani Y, Yip S. Phys Rev B 2004;70(10):104104.
[16] Shen S, Atluri SN. CMES 2004;6(1):91–104.
[17] Delph TJ. Proc Roy Soc Lond Ser A 2005;461(2058):1869–88.
[18] Heinz H. Mol Simul 2007;33(9):747–58.
[19] Gullett PM, Horstemeyer MF, Baskes MI, Fang H. Modell Simul Mater Sci Eng 2008;16(1):015001.
[20] Zimmerman JA, Webb III EB, Hoyt JJ, Jones RE, Klein PA, Bammann DJ. Modell Simul Mater Sci Eng 2004;12(4):S319–32.
[21] Zimmerman JA, Bammann DJ, Gao H. Int J Solids Struct 2009;46(2):238–53.
[22] Hoover WG, Hoover CG, Lutsko JF. Phys Rev E 2009;79(3):036709.
[23] Cormier J, Rickman JM, Delph TJ. J Appl Phys 2001;89(1):99–104.
[24] Irving JH, Kirkwood JG. J Chem Phys 1950;18(6):817–29.
[25] Szefer G. Comput Sci 2004;14:541–8.
[26] Sun ZH, Wang XX, Soh AK, Wu HA. Modell Simul Mater Sci Eng 2006;14(3):423–31.
[27] Root S, Hardy RJ, Swanson DR. J Chem Phys 2003;118(7):3161–5.
[28] Wajnryb E, Altenberger AR, Dahler JS. J Chem Phys 1995;103(22):9782–7.
[29] Delph TJ. Modell Simul Mater Sci Eng 2005;13:585–94.
[30] Webb III EB, Zimmerman JA, Seel SC. Math Mech Solids 2006;13(3):221–66.
[31] Hager WW, Zhang H. SIAM J Optim 2005;16(1):170–92.
[32] Pacheco AA, Batra RC. J Mech Phys Solids 2008;56:3116–43.
[33] Batra RC, Pacheco AA. Comput Mater Sci 2009;46:960–76.
[34] Subramaniyan AK, Sun CT. Int J Solids Struct 2008;45:4340–6.
[35] Jiang W, Batra RC. Acta Mater 2009;57:4921–32.
[36] Pu Q, Leng Y, Tsetseris L, Park HS, Pantelides ST, Cummings PT. J Chem Phys 2007;126:144707.
[37] Voter F, Chen SP. Characterization of defects in materials. In: Siegel RW, Weertman JR, Sinclair R, editors. Materials Research Society symposium proceedings, vol. 82. Pittsburgh: Materials Research Society; 1987. p. 175.
[38] Ercolessi F, Parrinello M, Tosatti E. Philos Mag A 1998;58:213.
[39] Rubio-Bollinger G, Bahn SR, Agzair N, Jacobsen KW, Vieira S. Phys Rev Lett 2001;87:026101.
[40] Sen D, Buehler MJ. Phys Rev B 2008;77:195439.